In silico investigations of intratumoral heterogeneous interstitial fluid pressure

Jahn Otto Waldeland [a], Jon-Vidar Gaustad [b], Einar K. Rofstad [b], Steinar Evje [a,*]

[a] University of Stavanger, Faculty of Science and Technology, NO-4068 Stavanger, Norway
[b] Department of Radiation Biology, Institute for Cancer Research, Oslo University Hospital, Oslo, Norway

ABSTRACT

Recent preclinical studies have shown that interstitial fluid pressure (IFP) within tumors can be heterogeneous Andersen et al. (2019). In that study tumors of two xenograft models, respectively, HL-16 cervical carcinoma and Panc-1 pancreatic carcinoma, were investigated. Significant heterogeneity in IFP was reported and it was proposed that this was associated with division of tissue into compartments separated by thick connective tissue bands for the HL-16 tumors and with dense collagen-rich extracellular matrix for the Panc-1 tumors. The purpose of the current work is to explore these experimental observations by using in silico generated tumor models. We consider a mathematical multiphase model which accounts for tumor cells, fibroblasts and interstitial fluid. The model has been trained to comply with experimental *in vitro* results reported in Shieh et al. (2011) which has identified autologous chemotaxis, ECM remodeling, and cell-fibroblast interaction as drivers for invasive tumor cell behavior. The in silico model is informed with parameters that characterize the leaky intratumoral vascular network, the peritumoral lymphatics which collect the fluid, and the density of ECM as represented through the hydraulic conductivity of the interstitial space. Heterogeneous distribution of solid stress may result in heterogeneous compression of blood vessels and, thus, heterogeneous vascular density inside the tumor. To mimic this we expose the in silico tumor to an intratumoral vasculature whose net effect of density of blood vesssels and vessel wall conductivity is varied through a 2D Gaussian variogram constrained such that the resulting IFPs lie within the range as reported from the preclinical study. The in silico cervical carcinoma model illustrates that sparse ECM was associated with uniform intratumoral IFP in spite of heterogeneous microvascular network, whereas compartment structures resulted in more heterogeneous IFP. Similarly, the in silico pancreatic model shows that heterogeneity in the microvascular network combined with dense ECM structure prevents IFP to even out and gives rise to heterogeneous IFP. The computer model illustrates how a heterogeneous invasive front might form where groups of tumor cells detach from the primary tumor and form isolated islands, a behavior which is natural to associate with metastatic propensity. However, unlike experimental studies, the current version of the in silico model does not show an association between metastatic propensity and elevated IFP.

© 2021 The Author(s). Published by Elsevier Ltd. This is an open access article under the CC BY license (http://creativecommons.org/licenses/by/4.0/).

1. Introduction

1.1. PDAC characteristics

Pancreatic ductal adenocarcinoma (PDAC) patients develop lymph node metastases early and have a particularly poor prognosis. Most PDACs are resistant to chemotherapy and radiation treatment (Castellanos et al., 2011) and surgery is the only treatment modality that may result in cure (Winter et al., 2012). Metastatic spread into and through lymphatics and lymph nodes occurs frequently in PDAC patients. The microenvironment of PDACs is characterized by an abundant desmoplastic stroma that may occupy up to 80% of the tumor volume (Whatcott et al., 2015; Bijlsma and van Laarhoven, 2015; Feig et al., 2012). The PDAC stroma consists of a dynamic assortment of extracellular matrix components including fibronectin, collagen, proteoglycans, and hyaluronic acid, nonmalignant cells including fibroblasts, endothelial cells, and immune cells, and soluble proteins such as growth factors and cytokines (Feig et al., 2012). Recent investigations have revealed that the PDAC stroma represents a physical barrier to the delivery of chemotherapeutic agents and simultaneously supports tumor growth and promotes metastatic dissemination (Whatcott et al., 2015; Bijlsma and van Laarhoven, 2015; Feig et al., 2012). The

---

* Corresponding author.
  E-mail address: steinar.evje@uis.no (S. Evje).

development of an abundant stroma during tumor growth distorts the architecture of the normal pancreas, resulting in an abnormal configuration of blood vessels and lymphatics in PDACs (Mahadevan and Von Hoff, 2007; Fink et al., 2016). Geometric resistance to blood flow is high in microvascular networks showing high fractions of low-diameter vessels, resulting in elevated microvascular pressure. Preclinical and clinical investigations have revealed that PDACs may show highly elevated interstitial fluid pressure (IFP) (Provenzano et al., 2012; Chauhan et al., 2014; DuFort et al., 2016) as well as high fractions of hypoxic tissue (Dhani et al., 2015; Dhani et al., 2015). The dense desmoplastic stroma has been suggested to be a determinant of the aggressive metastatic growth of PDACs (Whatcott et al., 2015; Bijlsma and van Laarhoven, 2015; Feig et al., 2012). There is some evidence that PDAC metastasis is promoted by direct interactions between the parenchymal tumor cells and the cellular and/or matrix components of the stroma (Singh et al., 2015; Fokas et al., 2015). It has been searched for associations between lymph node metastasis and features of the physicochemical microenvironment in an attempt to identify mechanisms leading to metastatic dissemination and growth. Two different xenografts were used as preclinical models of human PDAC in Andersen et al. (2017). In both models, lymph node metastasis was associated with high IFP rather than high fraction of hypoxic tissue or high microvascular density.

1.2. Cervical carcinoma characteristics

The most important tumor-related prognostic factors for cervical carcinoma are tumor volume, stage of disease, and lymph node status (Klopp and Eifel, 2012). During growth, cervical carcinomas develop a highly hostile physicochemical tumor microenvironment characterized by severe hypoxia, interstitial hypertension, low microvascular density, low extracellular pH, high lactate concentration, low glucose concentration, and energy deprivation (Höckel and Vaupel, 2001; Vaupel and Kelleher, 2012). This microenvironment causes treatment resistance and promotes malignant progression of the disease, and during the last decade, it has become increasingly clear that the prognostic and predictive values of these microenvironmental abnormalities are significant. Thus, extensive hypoxia in the primary tumor has been shown to be associated with locoregional treatment failure and poor disease-free and overall survival rates in patients with advanced disease (Höckel et al., 1993; Höckel et al., 1996; Fyles et al., 1998; Sundfør et al., 2000). Studies of cervical carcinoma patients treated with radiation therapy alone have shown that high interstitial fluid pressure (IFP) in the primary tumor is linked to high probability of pelvic recurrence and distant metastases (Milosevic et al., 2001; Fyles et al., 2006; Yeo et al., 2009). Moreover, the disease-free and overall survival rates have been shown to be particularly poor for cervical cancer patients with high lactate concentration in the primary tumor (Schwickert et al., 1995; Walenta et al., 2000). Interestingly, Fyles et al. (2006) have measured both IFP and oxygen tension in the primary tumor of more than 100 patients with advanced cervical carcinoma, and their study showed no correlation between either IFP or hypoxic fraction and established tumor-related prognostic factors. Furthermore, they observed that the independent prognostic effect of IFP for recurrence and survival was strong, whereas the independent prognostic effect of tumor hypoxia was of borderline significance and was limited to patients without nodal metastatic growth (Fyles et al., 2006).

1.3. CAFS

Fibroblasts in normal tissue are usually single cells residing in the interstitial space. Fibroblasts are non-epithelial and non-immune cells which likely originate from a mesenchymal lineage

(Croft, 1969). Fibroblasts that are recruited into tumor masses, called tumor-associated fibroblasts (TAFs) or cancer-associated fibroblasts (CAFs), are the main cellular components of the surrounding stroma of many solid cancers. Evidently, these CAFs provide a range of different cytokines, growth factors, tissue remodeling enzymes and ECM components, all of which regulate the tumor stroma (Desmouliere et al., 2004; Kalluri and Zeisberg, 2006). Gaggioli et al. (2007) discovered that fibroblasts may act as leader cells of a collective group of following carcinoma cells. This would allow cancer cells to retain their epithelial features, which is observed in solid tumors *in vivo* and also *in vitro* (Zheng et al., 2015; Fischer et al., 2015), while having a mesenchymal-like cell to lead them to invade the adjacent stroma. Furthermore, Gaggioli proposed that cancer cells move within paths behind fibroblasts. These paths are created by the fibroblasts both through proteolytic activity and force-mediated matrix remodeling (Barbazán and Vignjevic, 2019). Fibroblast-enhanced tumor cell migration was investigated by Shieh et al. in the presence of interstitial flow where, similar to Gaggioli et al., the fibroblasts created tracks within the ECM for cancer cells to follow (Shieh et al., 2011). Later, Labernadie et al. identified another possible mechanism to which fibroblasts lead cancer cells, a heterotypic cell–cell adhesion between the two types of cell. More specifically, there is a direct mechanical coupling between the fibroblast N-cadherin and the tumor cell E-cadherin (Labernadie et al., 2017). These two mechanisms have been accounted for and are the subject of investigations through a mathematical model in Urdal et al. (2019) and Waldeland et al. (2020) based on a cell-fibroblast-fluid multiphase formulation. In Urdal et al. (2019) the proposed cell-fibroblast-fluid model was trained with data from the *in vitro* experiments reported in Shieh et al. (2011). A first version of an in silico version of the model was explored in the recent work (Waldeland et al., 2020) where focus was on demonstrating how tumor cells can invade adjacent tissue by using fibroblasts as leader cells. Motivated by the results of Labernadie et al. (2017) direct mechanical interaction between fibroblasts and tumor cells are included in the computer model. In addition, the in silico model accounts for the mechanism that moving fibroblasts may remodel ECM, causing tumor cells to migrate in the tracks of ECM created by the fibroblasts, as observed in Gaggioli et al. (2007), Shieh et al. (2011), Schwager et al. (2019).

1.4. Motivation and objective

The purpose of the study reported in Hansem et al. (2019) was to determine whether tumors may show significant heterogeneity in IFP in the central region, and moreover, to reveal whether any heterogeneity may have consequences for the assessment of microenvironment-induced tumor aggressiveness. The study was based on the hypothesis that heterogeneous IFP in the central tumor region, if present, to a large extent is caused by structures that prevent efficient fluid flow in the interstitial space (i.e., related to tissue conductivity) in combination with the distorted intratumoral vasculature caused by solid stress. Detailed comparative studies of IFP and tumor histology were carried out using preclinical tumor models, respectively, HL-16 cervical carcinoma xenografts and Panc-1 pancreatic carcinoma xenografts, known to show significant intertumor heterogeneity of the extracellular matrix. At the same time, the occurence of lymph node metastasis was assessed as a measure of the tumor aggressiveness. It was found that when IFP of HL-16 and Panc-1 was measured at two different positions in the tumor center, the values could differ by a factor of up to 1.5 in both tumor models. Moreover, the propensity of the tumors to develop lymph node metastases was associated with the higher but not with the lower of the two IFP values. We are interested in an in silico tumor model that can shed light on

the observations from studying these preclinical models (Hansem et al., 2019). Central questions are: (i) Can the in silico model explain the homogeneous IFP observed for HL-16 cervical carcinoma when ECM is without compartments and Panc-1 pancreatic carcinoma when ECM is sparse? (ii) Can the in silico model explain the IFP heterogeneity observed for cervical carcinoma when compartments are present? And why should the dense ECM structure for pancreatic carcinoma give rise to IFP heterogeneity? (iii) How does tumor cell invasive migration respond to heterogeneities associated with the ECM structure and the corresponding IFP?

1.5. Review of some previous modeling

Different models have their own possibilities and limitations, strengths and weaknesses. The models apply different assumptions regarding which effects to represent explicitly and which effects to account for in a more implicit manner. In the following we review some models that have been explored more lately and also played a role in shaping the model used in this work. In Wu et al. (2013) a multiphase approach was used to explore the critical role played by interstitial fluid (IF) and associated interstitial fluid pressure (IFP) in solid tumors. A continuous growth model was coupled with a discrete model for angiogenesis. The role of oxygen and fluid extravasation was explicitly accounted for. The authors investigated how nonlinear interactions among the vascular and lymphatic networks and proliferating tumor cells may influence IFP, transport of oxygen, and tumor progression. The fluid flow is represented by Darcy's law, implying that the IFP is a result of the draining fluid produced by the leaky blood vasculature and collected by the lymphatic system, and the resistance represented through the tissue conductivity. Solid stress associated with the growing tumor is accounted for through the hydrostatic tumor pressure via a Darcy like equation for the solid phases. The interstitial hydraulic conductivity in the tumor is related to the tumor ECM density, i.e., higher (lower) hydraulic conductivity is associated with lower (higher) ECM density. The model has been extended to account for delivery of an anticancer drug via the blood vasculature (Wu et al., 2014). In Frieboes et al. (2010) a dynamic evolving tumor vasculature is combined with multispecies tumor invasion driven by an interplay between a proliferating phenotype and a migrating phenotype. The model is based on mass balance equations for each species and corresponding generalized Darcy laws for the various components where coefficients involve mobility functions that reflect the combined effects of cell–cell and cell-matrix adhesion. The model has been used in the context of Glioblastoma (Yan et al., 2017) to explore tumor progression and response to anticancer drug. In Jarrett et al. (2020, 2018) and Jarrett et al. (2018) an experimental-mathematical framework on tissue level is used to integrate quantitative magnetic resonance imaging (MRI) data into a biophysical model to predict patient-specific treatment response of locally advanced breast cancer to neoadjuvant therapy. Effects accounted for in the mathematical model are migration by diffusion where the nonlinear diffusion coefficient is coupled to stress calculations, proliferation/apoptosis with a proliferation rate coefficient which is estimated, and an anti-cancer term that eradicates cancer cells by contact. A family of biophysical models of tumor growth and angiogenesis have been developed that are calibrated with diffusion-weighted magnetic resonance imaging and dynamic contrast-enhanced MRI data to provide individualized tumor growth forecasts (Hormuth et al., 2019). The tumor cells as well as the evolution of the blood vasculature are described by using two diffusion–reaction equations.

Another, but related type of mathematical model of tumor growth on tissue level has been formulated in Mpekris et al. (2015) for the purpose of exploring interconnections among

(i) tumor oxygenation;
(ii) the heterogeneous accumulation of mechanical stresses owing to tumor growth;
(iii) the non-uniform compression of intratumoral blood vessels due to the mechanical stresses;
(iv) and the insufficient delivery of oxygen and therapeutic agents because of vessel compression.

The authors found that the high vascular density and increased cancer cell proliferation often observed in the periphery can be attributed to heterogeneous solid stress accumulation. The mathematical model was based on a biphasic formulation in terms of volume fractions that account for solid phase and fluid phase with corresponding different velocities. Source terms associated with these mass balance equations account, respectively, for the growth of the solid phase and the drainage of the IF from the leaky tumor vasculature and collected by the lymphatics through Starling's law. A Darcy type equation is used where the difference between solid and fluid velocity is linearly related to the IF pressure gradient with the hydraulic conductivity of the tissue as coefficient. A similar model was used in Angeli and Stylianopoulos (2016) to evaluate the effect of radiation therapy.

A mathematical model for tumor progression is considered in Mascheroni et al. (2019) which accounts for microenvironmental changes that might trigger chemo-mechanically induced cellular phenotypic transitions. The model is based on diffusion-reaction equations to describe migrating cancer cells, vascularity density and nutrient whereas the proliferating cells are represented by an ordinary differential equation (ODE). An algebraic equation is used to represent mechanical compression of the cells in a phenomenological way. Reaction terms are included to model that phenotypic transitions of tumor cells are driven by both chemical and mechanical effects. A phenotypic transition driven by mechanical pressure is assumed, i.e., compression favors cell migration and inhibits cell proliferation. The authors analyze the effects of mechanical compression on the internal balance between migration and proliferation of glioma cells and the impact on tumor infiltration. In Lewin et al. (2020) a three-phase multiphase model is explored, similar to previous models (Hubbard and Byrne, 2013; Breward et al., 2002; Byrne et al., 2003), which involves three separate mass balance equations and corresponding momentum balance laws. General momentum balance equations are used where also external force terms are accounted for. The different phases are tumor cells, dead cellular material, and fluid. Through numerical simulation of the model equations, spatial structures and dynamics typical of those associated with the growth of avascular tumour spheroids are investigated.

A biphasic tumor model is used in Mascheroni et al. (2016) that accounts for the tumor cells and the interstitial fluid. Mechanical stress on the solid phase (cancer cells) is described by an effective stress tensor and involves a stress term from IF (isotropic IFP) with inclusion of Biot's coefficient and a total stress tensor in the tissue (matrix/ECM). The effective stress tensor for the solid phase is given in terms of an isotropic constitutive term (elastic fluid) which expresses that for low volume fraction of cancer cells, they tend to attract, for high they tend to repel (Byrne and Preziosi, 2003). In Mascheroni et al. (2017), the model in Mascheroni et al. (2016) is combined with governing equations for transport and uptake of a chemotherapeutic agent, acting on cell proliferation. Model simulations suggest that mechanical compression of tumors may imply that a drug dose that is effective in reducing tumor volume for stress-free conditions may not perform equally well in a mechanically compressed environment. Finally, in d'Esposito et al. (2018) a 3D mathematical model is explored which combines a steady state model for vascular flow, IFP, and interstitial fluid, and a transient model for delivery of a chemical agent through

the vasculature. The steady-state model relies on combining a network model (similar to Wu et al., 2013; Wu et al., 2014) with single-phase Darcy's law and Starling's law for describing the exchange of fluid between vasculature and interstitium. It is demonstrated that by adding realistic, whole-tumor microstructure with its inherent heterogeneity, accurate predictions of fluid mechanical aspects of the tumor and delivery of chemical agents can be achieved.

2. Mathematical model

The mathematical model we use to represent the solid tumors bears many similarities with previous models. However, motivated by recent results which emphasize the possible role played by fluid flow and related forces as a means for cancer cells to seed distant metastases (Follain et al., 2020), we will inform the model with experimentally observed fluid-sensitive migration mechanisms, both for fibroblasts and cancer cells. The proposed model has some novel features in that respect, to the best of our understanding. In the following we briefly highlight some similarities and differences to multiphase models explored by other researchers (Breward et al., 2002; Byrne et al., 2003; Hubbard and Byrne, 2013; Wu et al., 2013; Wu et al., 2014; Mascheroni et al., 2016; Mascheroni et al., 2017; d'Esposito et al., 2018; Lewin et al., 2020; Mpekris et al., 2015; Angeli and Stylianopoulos, 2016; Weis et al., 2015; Jarrett et al., 2018; Hormuth et al., 2019). One main focus is on the coupling between the heterogeneous IF drainage and IFP and the corresponding aggressive and invasive cancer cell behavior at the tumor periphery.

2.1. Underlying assumptions and principles for the mathematical multiphase model

1. We consider three separate phases in terms of cancer cells α_c, fibroblasts (CAFs) α_f and interstitial fluid α_w which are represented through separate mass balance equations and momentum balance equations which account for the stress tensor and external forces for each individual phase (Hubbard and Byrne, 2013; Lewin et al., 2020).
2. Cancer cells and CAFs are able to generate friction forces and active traction forces (Alert and Trepat, 2020). To represent these mechanisms the tissue is considered as a porous medium composed of a stagnant, rigid solid matrix that essentially represents the ECM structures whereas the porous space is available for the cancer cells, CAFs and fluid to move through. This is accounted for through a porosity ϕ. The momentum balance laws explicitly represent interaction forces between cancer cells and CAFs as well as resistance forces (friction) between the different phases and underlying matrix. This allows to account for fluid-sensitive migration mechanisms (Follain et al., 2020) as reported in Shieh et al. (2011), Polacheck et al. (2011), Urdal et al. (2019) that might play a role in invasive behavior and metastasis during tumor progression (Waldeland et al., 2020). In particular, the momentum balance for IF involves a Darcy-type model as used by others (Wu et al., 2013, 2014) who have explored how the elevated intratumoral IFP is a result of the tissue conductivity and aberrant intratumoral vasculature caused by solid stress (Mpekris et al., 2015; Angeli and Stylianopoulos, 2016).
3. The intratumoral blood and lymphatic vasculature are modeled by using a continuum approach based on Starling's law (Wu et al., 2013; Wu et al., 2014; Mpekris et al., 2015). However, we do not explicitly account for angiogenesis and dynamic changes in the fluid drainage, as done by others. When we simulate the tumor progression during a period of some days, we set the net effect of proliferation and apoptosis to be zero since proliferation is associated with an evolving vasculature. We could include such effects but have chosen not to do so since our motivation is to focus more precisely on how fluid-sensitive migration mechanisms (Shieh et al., 2011; Polacheck et al., 2011) might be a driver for invasive behavior and metastatic dissemination of cancer cells.
4. We explicitly account for solid stress through P_c and P_f, respectively, associated with cancer cells and fibroblasts, similar to what is done in Frieboes et al. (2010), Wu et al. (2013), Hubbard and Byrne (2013), Lewin et al. (2020), Mascheroni et al. (2016), Mascheroni et al. (2017). More precisely, $P_c = P_w + \Delta P + \Lambda$ where P_w is IFP and ΔP and Λ represent stress generated by the moving cancer cells as they interact with the surrounding ECM structure through diffusive spreading and chemotactic migration, respectively, The external interaction force terms are also involved in this build-up of solid stress. To mimic that heterogeneous distribution of solid stress may result in heterogeneous vascular density inside the tumor (Mpekris et al., 2015), the effective coefficients involved in Starling's law are varied as a 2D Gaussian variogram (in space) from one tumor to another. Similarly, we also generate a heterogeneous lymphatic network in the peritumoral region.
5. Solid stress may facilitate fibroblasts activation which in turn promotes pancreatic cancer cell migration (Kalli et al., 2018). Compressed fibroblasts continuously interact with cancer cells and induce cancer cell migration possibly through secretion of fibroblasts-derived factors (Desmouliere et al., 2004; Kalluri and Zeisberg, 2006). This is accounted for in the model by letting the CAFs represent a phenotype with activated migration abilities. Also the dense ECM structure, which affects the tissue conductivity (Wu et al., 2013) as well as intratumoral vasculature might be a result of this solid stress-stimulated fibroblast activation.
6. Solid stress is reported to be a driver for the development of the aberrant intratumoral vasculature with high intravascular pressure and high vasculature conductivity reflecting a high degree of leaky walls (Jain et al., 2014). Solid stress may also suppress proliferation and promote cancer cell phenotype with higher degree of viability (Frieboes et al., 2010; Jain et al., 2014; Mascheroni et al., 2019). Similarly, it has been found that interstitial fluid flow inhibits the proliferation for a pancreatic cell line while a high viability is maintained (de Haan et al., 2019). This motivates for our assumption that the cancer cell is a phenotype where proliferation has been down-graded and migration upgraded.
7. For evaluation of the simulation outputs, we first generate an ensemble of input parameters that characterizes (through Starling's law) the heterogeneous intratumoral vasculature and peritumoral lymphatic network, as well as tissue conductivity. We use literature values for these parameters to represent their means combined with stochastic-generated variations constrained such that the resulting intratumoral IFP is consistent with measured values reported in Hansem et al. (2019). A motivation for this approach is that it represents the first step in an assimiliation-based method (Aanonsen et al., 2009) where observed data (e.g., from MRI) can be used to calibrate model parameters (Jarrett et al., 2018; Hormuth et al., 2019).

2.2. Cell-fibroblast-fluid model

A brief presentation of the model is given as details can be found elsewhere (Urdal et al., 2019; Waldeland et al., 2020) (Appendix A). Note that ϕ is the volume fraction occupied by the pore space through which the cells and fluid can move whereas

$1 - \phi$ represents the remaining matrix volume fraction. The mathematical model takes the following form using variables as summed up in Table 1:

$$
\begin{aligned}
&(\phi\alpha_c)_t + \nabla \cdot (\phi\alpha_c\mathbf{u}_c) = S_c \\
&(\phi\alpha_f)_t + \nabla \cdot (\phi\alpha_f\mathbf{u}_f) = S_f, \qquad \alpha_c + \alpha_f + \alpha_w = 1 \\
&(\phi\alpha_w)_t + \nabla \cdot (\phi\alpha_w\mathbf{u}_w) = -S_c - S_f + Q, \quad Q = Q_v - Q_l \\
&\alpha_c\nabla(P_w + \Delta P_{cw} + \Lambda_C) = -\hat{\zeta}_c\mathbf{u}_c + \hat{\zeta}_{cf}(\mathbf{u}_f - \mathbf{u}_c) \\
&\alpha_f\nabla(P_w + \Delta P_{fw} + \Lambda_H) = -\hat{\zeta}_f\mathbf{u}_f - \hat{\zeta}_{cf}(\mathbf{u}_f - \mathbf{u}_c) \\
&\alpha_w\nabla P_w = -\hat{\zeta}_w\mathbf{u}_w \\
&(\phi\alpha_w C)_t = \nabla \cdot (D_C\nabla C) - \nabla \cdot (\phi\alpha_w C\mathbf{u}_w) + Q_C \\
&(\phi\alpha_w H)_t = \nabla \cdot (D_H\nabla H) - \nabla \cdot (\phi\alpha_w H\mathbf{u}_w) + Q_H
\end{aligned}
\tag{1}
$$

where $\mathbf{u}_i = (u_i^x, u_i^y)$ for $i = c, f, w$. Since ϕ is here assumed to be constant it can be incorporated in the dimensionless time and grouped with the velocities $\mathbf{u}_c, \mathbf{u}_f, \mathbf{u}_w$ (Waldeland et al., 2020) (Appendix A). Eq. $(1)_{1-3}$ represent, respectively, the mass balance equations for cancer cells, fibroblasts and interstitial fluid. The next three equations, $(1)_{4-6}$, are the corresponding momentum balance equations (Hubbard and Byrne, 2013; Lewin et al., 2020). The RHS of $(1)_4$ is separated into two terms: $-\hat{\zeta}_c\mathbf{u}_c$ represents the resistance against migration felt by cancer cells from the ECM whereas $\hat{\zeta}_{cf}(\mathbf{u}_f - \mathbf{u}_c)$ represents the interaction force between fibroblasts and cancer cells. Here we have ignored a cell-fluid interaction term of the form $\pm\hat{\zeta}_{cw}(\mathbf{u}_w - \mathbf{u}_c)$, respectively, in $(1)_4$ and $(1)_6$. This is based on the experimental finding that cancer cells did not enhance migration due to fluid flow alone, only in the presence of both fluid flow and chemotaxis (Shieh et al., 2011). For the same reason, the fibroblast-fluid interaction term $\pm\hat{\zeta}_{fw}(\mathbf{u}_w - \mathbf{u}_f)$ is also ignored, respectively, in $(1)_5$ and $(1)_6$ (Urdal et al., 2019). For a theoretical justification we refer to Giverso et al. (2015). Solid stress associated with the cell phase is $P_c = P_w + \Delta P_{cw} + \Lambda_C$, similar to what has been used by others (Frieboes et al., 2010; Wu et al., 2013; Hubbard and Byrne, 2013; Lewin et al., 2020; Mascheroni et al., 2016; Mascheroni et al., 2017). Herein, $\Delta P_{cw}(\alpha_c)$ quantifies a stress in the cell phase associated with a diffusive migration. The potential function $\Lambda_C(C)$ represents additional stress that accounts for chemotaxis toward higher concentrations of chemokine C. Similarly, the RHS of $(1)_5$ accounts for fibroblast-ECM interaction and cell-fibroblast interaction, respectively, whereas solid stress associated with the fibroblasts is $P_f = P_w + \Delta P_{fw} + \Lambda_H$. Herein, $\Delta P_{fw}(\alpha_f)$ accounts for diffusive migration whereas the potential function $\Lambda_H(H)$ accounts for

chemotaxis of fibroblasts towards positive gradients in growth factor H. The fluid momentum balance through $(1)_6$ amounts to Darcy's law (Wu et al., 2013; Wu et al., 2014; d'Esposito et al., 2018). The two remaining equations, $(1)_{7,8}$, are transport-reaction equations for chemokine and TGF, respectively. Rate terms for production/decay of C and H are given by Q_C and Q_H and are specified in Table 2. The values used for different rate terms λ_{ij} are given in Table 8 (Appendix) and is based on the calibration done in Urdal et al. (2019) to mimic the experimental results reported in Shieh et al. (2011).

Remark 2.1. The description of how chemokine is produced has been simplified in the model (1) as compared to previous versions of the model (Urdal et al., 2019; Waldeland et al., 2020). This allows us to reduce the number of variables and parameters involved in corresponding rate equations and at the same time maintain the essential mechanism as reported from experimental work (Shieh et al., 2011). Namely, that chemokine and growth factor are transported by the fluid velocity field and tend to accumulate nearby peritumoral lymphatic vessels which drain the excess fluid.

2.3. Interaction coefficients

The interaction coefficients $\hat{\zeta}_w, \hat{\zeta}_c, \hat{\zeta}_f$, and $\hat{\zeta}_{cf}$ which are used in $(1)_{4-6}$ are as follows (Urdal et al., 2019; Waldeland et al., 2020; Qiao et al., 2018; Qiao and Evje, 2020):

$$
\hat{\zeta}_w = I_w\hat{k}_w\phi\alpha_w^{r_w}, \qquad \hat{\zeta}_c = I_c\hat{k}_c\phi\alpha_c^{r_c}, \qquad \hat{\zeta}_f = I_f\hat{k}_f\phi\alpha_f^{r_f},
$$
$$
\hat{\zeta}_{cf} = I_{cf}\phi\alpha_c^{r_{cf}}\alpha_f^{r_{fc}}.
\tag{2}
$$

The parameters I_w, I_c and I_f (Pas/m^2) represent static properties of the tissue, whereas $\hat{k}_w, \hat{k}_c$ and $\hat{k}_f$ (dimensionless) can account for dynamic properties related to for instance ECM remodeling and fiber alignment or various ECM heterogeneities (Shieh et al., 2011). The coefficients r_w, r_c, r_f, r_{cf} and r_{fc} (dimensionless) play a similar role to the use of relative permeability functions in standard Darcy's equation approach extended to several phases (Evje, 2017; Qiao et al., 2018; Qiao and Evje, 2020). I_{cf} is a constant determining the order of magnitude of the cell-fibroblast interaction. We use $I_{cf} = 1000I_w$ to describe how strongly the cancer cells are mobilized through their interaction with surrounding fibroblasts. As I_{cf} becomes larger, the difference between fibroblast and cancer cell velocity becomes smaller, ultimately converging toward zero (Urdal et al., 2019). We assume that fibroblasts remodel and degrade the ECM, making it easier for the cancer cells to migrate in their path. This is represented through the following equation:

$$
\hat{k}_c = 1 - A(1 - \exp(-B\alpha_f)), \qquad (A, B \text{ are dimensionless constants}).
\tag{3}
$$

The values used for the different parameters involved in (2) and (3) are presented in Table 7 (Appendix A). These are based on the calibration done in Urdal et al. (2019) to mimic the experimental results reported in Shieh et al. (2011). Compared to previous use of the model (1), we have to account for band-like structures in

Table 1
Variables used in the model (1).

Variable	Description
$\phi, \alpha_c, \alpha_f, \alpha_w$	Tissue porosity, volume fraction of cell, fibroblast, fluid
S_c, S_f	cell growth/death
$\mathbf{u}_c, \mathbf{u}_f, \mathbf{u}_w$	interstitial cell, fibroblast and fluid velocity
C, H	chemokine, TGF
P_w, P_c, P_f	IF pressure, solid stress associated with cancer cell, fibroblast
$\Delta P_{fw}, \Delta P_{cw}, \Lambda_C, \Lambda_H$	caf-caf, cell–cell, chemokine, TGF chemotactic stress
$\hat{\zeta}_c, \hat{\zeta}_f, \hat{\zeta}_w, \hat{\zeta}_{cf}$	cell-ECM, fibroblast-ECM, fluid-ECM, cell-fibroblast interaction terms
Q_v, Q_l	produced fluid from leaky vasculature, collected fluid through lymphatics
T_v, T_l	effective conductivity of vascular vessel wall, lymphatic vessel wall
$\tilde{P}_v^*, \tilde{P}_l^*$	effective vascular pressure, lymphatic pressure
D_C, D_H	diffusion coefficients associated with C, H
Q_C, Q_H	production/decay rates associated with C, H
Ω_v, Ω_l	region of intratumoral vascular, peritumoral lymphatic network

Table 2
Source terms in $(1)_{7,8}$ accounting for production/decay of chemokine and growth factor.

Function		Description
Q_C	=	$\alpha_c\alpha_f\left(\lambda_{11} - \lambda_{12}\left(\frac{C}{C_M}\right)^{v_C}\right) - \lambda_{13}\alpha_c C - M_C Q_l C$
Q_H	=	$\alpha_f\left(\lambda_{21} - \lambda_{22}\left(\frac{H}{H_M}\right)^2 - \lambda_{23}\left(\frac{H}{H_M}\right)^{v_H}\right)$
		$- \lambda_{24}\alpha_f H - \lambda_{25}H - M_H Q_l H$

the ECM when we do simulations. This is done by generating band-like structures in the conductivity-related coefficient $\hat{k}_w$. Details are given in Section 3.

2.4. Starling law

In nearly all tissue, plasma leaks out of blood capillaries, flows through the interstitium and drains into lymphatic vessels, where it passes through lymph nodes before being returned to the venous blood (Jain et al., 2014). This circulation is expressed on the RHS of $(1)_3$ through the term $Q = Q_v - Q_l$. The main contributors to interstitial flow Q_v are hydrostatic and osmotic pressure gradients between the vascular and interstitial space. Starling Law is used for the flow of fluid into the interstitium given by Frieboes et al. (2010), Wu et al. (2013), Wu et al. (2014), Mpekris et al. (2015), Angeli and Stylianopoulos (2016), d'Esposito et al. (2018)

$$Q_v = T_v(P_v^* - P_w - \sigma_T(\pi_v^* - \pi_w)) = T_v\left(\widetilde{P}_v^* - P_w\right) \qquad T_v = L_v\frac{S_v}{V} \quad (4)$$

where $\widetilde{P}_v^* = P_v - \sigma_T(\pi_v^* - \pi_w)$. Here L_v is the hydraulic conductivity $(\mathrm{m}^2\mathrm{s/kg} = \mathrm{m/Pa\,s})$ of the vessel wall, $S_v/V\,(\mathrm{m}^{-1})$ the exchange area of blood vessel per unit volume of tissues V. P_v^* and P_w are the vascular and interstitial fluid pressure, π_v^* and π_w the osmotic pressure in the vascular and interstitial space, and σ_T the osmotic reflection coefficient for plasma proteins. The lymphatic system drains excessive fluid from the interstitial space and returns it back to the blood circulation, as expressed by Q_l. Tumor lymphatics in cancers are typically not functional in the intratumoral region (Jain et al., 2014; Wu et al., 2013; Wu et al., 2014). The loss of functionality is caused by compressive solid stress that is developed in tumors. Through this stress the intratumoral lymphatic vessels collapse, and therefore lymphatic flow is eliminated. Similar to the expression of Q_v in (4), we use an expression of the following form to express the absorption of fluid through the lymphatics

$$Q_l = T_l\left(P_w - \widetilde{P}_l^*\right), \qquad T_l = L_l\frac{S_l}{V}. \quad (5)$$

Here L_l is the hydraulic conductivity of the lymphatic vessel walls whereas S_l/V is the surface area of the lymphatic vessel per volume unit of tissues V and $\widetilde{P}_l^*$ is the effective lymphatic pressure.

2.5. Cancer cell and CAF velocities

From (1) an expression for the interstitial cell velocity $\mathbf{u}_c$, caf velocity $\mathbf{u}_f$, and IF velocity $\mathbf{u}_w$ can be derived (Urdal et al., 2019; Waldeland et al., 2020):

$$\mathbf{u}_c = \underbrace{\frac{\hat{f}_c}{\alpha_c}\mathbf{U}_T}_{(i)} - \underbrace{\frac{\hat{h}_1 + \hat{h}_2}{\alpha_c}\nabla(\Delta P_{cw}(\alpha_c))}_{(ii)} - \underbrace{\frac{\hat{h}_1 + \hat{h}_2}{\alpha_c}\nabla(\Lambda_C(C))}_{(iii)}$$

$$+ \underbrace{\frac{\hat{h}_2}{\alpha_c}\nabla\Lambda_H(H)}_{(iv)} + \underbrace{\frac{\hat{h}_2}{\alpha_c}\nabla(\Delta P_{fw}(\alpha_f))}_{(v)} \quad (6)$$

$$\mathbf{u}_f = \frac{\hat{f}_f}{\alpha_f}\mathbf{U}_T + \frac{\hat{h}_2}{\alpha_f}\nabla(\Delta P_{cw}(\alpha_c)) + \frac{\hat{h}_2}{\alpha_f}\nabla(\Lambda_C(C)) - \frac{\hat{h}_2 + \hat{h}_3}{\alpha_f}\nabla\Lambda_H(H)$$

$$- \frac{\hat{h}_2 + \hat{h}_3}{\alpha_f}\nabla(\Delta P_{fw}(\alpha_f)) \quad (7)$$

$$\mathbf{u}_w = \frac{\hat{f}_w}{\alpha_w}\mathbf{U}_T + \frac{\hat{h}_1}{\alpha_w}\nabla(\Delta P_{cw}(\alpha_c) + \Lambda_C(C))$$

$$+ \frac{\hat{h}_3}{\alpha_w}\nabla(\Delta P_{fw}(\alpha_f) + \Lambda_H(H)). \quad (8)$$

We refer to Table 6 (Appendix A) for more information related to the functions $\hat{f}_c, \hat{f}_f$, and $\hat{h}_1, \hat{h}_2, \hat{h}_3$. It follows that these functions depend directly on the correlations (2). The terms on the RHS of (6) represent different migration mechanisms, resulting in the overall velocity $\mathbf{u}_c$:

(i) Fluid-generated stress
(ii) Diffusive spreading
(iii) Chemotaxis of cells toward higher concentration gradients in chemokine
(iv) Migration due to fibroblast chemotaxis towards higher concentration gradients in TGF
(v) Migration due to fibroblast diffusion.

Fluid generated stress (i) represents a co-current transport effect, where the two phases of cancer cell and fluid move in the same direction. The next term (ii) represents diffusive migration of tumor cells whereas (iii) accounts for directional migration of tumor cells towards higher concentration of chemokine C. The two last terms (iv) and (v) represent CAF-dependent migration as a result of the mechanical interaction between cancer cells and fibroblasts, as fibroblasts move in the direction of higher concentration of TGF H and spread by diffusion, respectively.

Remark 2.2. In the current work the proposed model (1) has been constructed such that it can account for the experimental observed interplay between fibroblasts and cancer cells under the influence of the outgoing fluid flow field (Shieh et al., 2011). However, fibroblasts are also known to play a central role in remodelling of the ECM structure. Hence, an interesting and relevant research task could be to couple the fibroblast phase to remodelling of ECM. ECM structures are accounted for through the fluid-ECM interaction term $\hat{\zeta}_w$ suggesting that this term somehow should sense the fibroblast activity. Such effects are ignored in the current version of the cell-fibroblast-fluid model as focus is on exploring through a mathematical model how fibroblasts may act as leader cells of a collective group of following tumor cells (Gaggioli et al., 2007). In particular, we seek to put to a test the potential metastatic mechanism involved when cancer cells retain their epithelial features (Zheng et al., 2015; Fischer et al., 2015), while having a mesenchymal-like cell to lead them to invade the adjacent stroma.

2.6. Summary of the essential aspects of the in silico tumor model

We give a short summary of the mechanisms of the model which indicates how the model can represent different aspects mentioned in the introduction. The computer model has been trained to comply with experimental *in vitro* results reported in Shieh et al. (2011) which has identified autologous chemotaxis, ECM remodeling, and cell-fibroblast interaction as drivers for invasive tumor cell behavior. This was achieved by first setting the fluid-ECM resistance force through $\hat{\zeta}_w$ such that reasonable pathological values are obtained for IF velocity (i.e., $0.1 - 1\ \mu\mathrm{m/s}$) and IFP. Secondly, the cell-ECM resistance force coefficients $\hat{\zeta}_c$ and $\hat{\zeta}_f$ are set such that cancer cells and fibroblasts largely can resist the force from the flowing fluid in accordance with the experimental observations. Thirdly, parameters that determine the strength of the chemotactic migration of fibroblasts and cancer cells through Λ_C and Λ_H, respectively, as well as the internal cell-fibroblast interaction $\hat{\zeta}_{cf}$, are set such that the migration of fibroblasts and cancer cells can mimic the experimental results in Shieh et al. (2011). The parameters are given in Table 7 and 8 (Appendix A) and characterize the aggressiveness of the assumed cell phenotype. Moreover, the computer model is informed with data per-

taining to the leaky intratumoral microvascular network, the peritumoral collecting lymphatic network, and the density of ECM as represented through the hydraulic conductivity of the interstitial space motivated by observations from the xenograft models reported in Hansem et al. (2019). To comply for the situation that heterogeneous distribution of solid stress may result in heterogeneous compression of blood vessels and, thus, heterogeneous vascular density inside the tumor, we generate coefficients T_v and T_l through a 2D Gaussian variogram but constrained such that the resulting intratumoral IFP lies within a pathological reasonable range (Hansem et al., 2019). Main mechanisms that drive the tumor progression in (1) are:

- Fluid is produced from the leaky vascular system residing near the periphery of the initial tumor and is absorbed by lymphatics found in the region outside of the primary tumor, characterized by the source terms in $(1)_3$ given by $Q = Q_v - Q_l$. The resulting fluid flow field is directed from the vascular to the lymphatic system (Hompland et al., 2012; Wu et al., 2013; Wu et al., 2014; d'Esposito et al., 2018). Tumors develop elevated IFP because they show high resistance to blood flow (i.e., $\widetilde{P}_v^*$ in (4) is high), low resistance to transcapillary fluid flow (i.e., T_v in (4) is high), and impaired lymphatic drainage (i.e., Q_l in (5) is located to the peritumoral region).

- Growth factor H (TGF) is secreted by fibroblasts α_f and chemokine C is secreted from cancer cells combined with fibroblast activity, as described by $(1)_{7,8}$. These chemical components diffuse and advect with the fluid flow through $\mathbf{u}_w$, creating chemical gradients downstream of the flow (Shieh et al., 2011). Cancer cells and fibroblasts migrate towards positive gradients of their respective chemotactic chemical, chemokine C and transforming growth factor (TGF) H. Chemotaxis is represented through the potential functions Λ_C and Λ_H appearing in $(1)_{4,5}$. Hence, the model accounts for autologous chemotaxis which has been observed from *in vitro* experiments (Shieh et al., 2011; Polacheck et al., 2011; Polacheck et al., 2014) and proposed as a possible mechanism for guiding tumor cells toward lymphatics (Fink et al., 2016; Andersen et al., 2017; Hompland et al., 2012). Expression of the chemokine CCL21 in lymphatic vessels correlated with increased lymph node metastasis in pancreatic patients (Guo et al., 2013; Sperveslage et al., 2012), as did overexpression of CCR7 in pancreatic tumor cells *in vivo* (Sperveslage et al., 2012) and supports the choice of autologous chemotaxis as a driver for tumor cell dissemination in the computer model.

- A large resistance force is imposed on the cancer cells making it difficult for them to migrate on their own, i.e., the cell-ECM interaction coefficient $\hat{\zeta}_c$ in (2) takes a large value. This is necessary to rule out the unrealistic behavior that cancer cells move only due to the push from the flowing fluid (Waldeland and Evje, 2018). Fibroblasts, on the other hand, are considered much more mobile, e.g. due to the tumor induced solid stress (Kalli et al., 2018). Fibroblasts reduce the resistance to migration experienced by cancer cells through the functional form of $\hat{k}_c$ given by (3). Cancer cells may attach themselves onto fibroblasts and/or follow tracks where fibroblasts have migrated due to the diminished resistance in their wake. This yields a largely fibroblast-dependent cancer cell migration, consistent with experimental observations (Gaggioli et al., 2007; Shieh et al., 2011; Labernadie et al., 2017).

3. Results

The model (1)–(5) is combined with the boundary condition

$$P_w|_{\partial\Omega} = P_B^*, \quad \frac{\partial}{\partial v}C|_{\partial\Omega} = 0, \quad \frac{\partial}{\partial v}H|_{\partial\Omega} = 0, \quad t > 0 \tag{9}$$

where v is the outward normal on the domain $\partial\Omega$ with $\Omega = [0,2] \times [0,2]$ (dimensionless) and P_B^* is atmospheric pressure. The corresponding initial data are

$$\alpha_c(\mathbf{x}, t = 0) = \alpha_{c0}(\mathbf{x}), \quad \alpha_f(\mathbf{x}, t = 0) = \alpha_{f0}(\mathbf{x}),$$
$$C(\mathbf{x}, t = 0) = H(\mathbf{x}, t = 0) = 0. \tag{10}$$

For more details on the numerical method we use, we refer to Appendix B.

3.1. Initial volume fraction of fibroblasts and tumor cells

The initial volume fraction of tumor cells, i.e., the primary tumor is shown in Fig. 1(A). An example of the initial fibroblast distribution is illustrated in Fig. 1(B). (A) shows the primary tumor at time $t = 0$ having a cancer cell volume fraction equal to approximately 0.3 in the center and quickly decreasing towards the periphery. This can be considered an ideal tumor whose margin is smooth and has no heterogeneity or indication of metastatic propensity. The fibroblast volume fraction in (B) is somewhat heterogeneous. Fibroblasts are assumed to surround the tumor in a bandlike region (Von Ahrens et al., 2017; Lakiotaki et al., 2016). The fibroblast volume fraction is generated randomly as a Gaussian
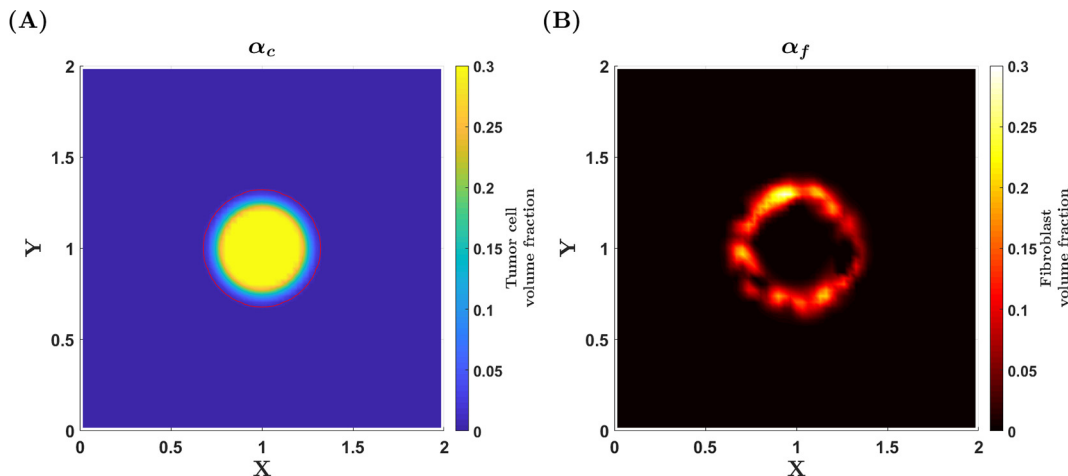
Fig. 1. Tumor cell and fibroblast status when the simulation of the in silico tumor model starts. **(A)** Initial cancer cell volume fraction. It is assumed the tumor is an ideal tumor, having a constant volume fraction of 0.3. The red contour line shows a volume fraction of 0.01. **(B)** Initial fibroblast volume fraction. The distribution of fibroblasts are generated through a Gaussian variogram, yielding random volume fractions around the tumor.

variogram in 2-D since this represents information related to the ECM status that is not accessible. Simulations are done subject to the condition that the net effect of cell proliferation/apoptosis is zero, i.e., $S_c = S_f = 0$ in $(1)_{1,2,3}$. This amounts to a situation where, e.g., solid stress may suppress proliferation and promote cancer cell phenotype with higher degree of viability (Frieboes et al., 2010; Mascheroni et al., 2019). Simulations are done by using a grid of 61×61 numerical grid blocks.

3.2. Model input parameters

The workflow when we apply the in silico tumor model is composed of two steps: (i) First, we assume that the tumor cells are equipped with migration mechanisms as found from *in vitro* studies (Shieh et al., 2011) as discussed in Urdal et al. (2019) and reflected by (6) and (7).

The chosen set of parameters found in Table 6–8 (Appendix A) may be considered as characteristic for the aggressiveness of the assumed phenotype.

These parameters are kept fixed, except that we will vary the parameters $\{\lambda_{2i}\}_{i=1}^5$ involved in $(1)_8$ (see Table 2) which control the preduction/consumption of the growth factor H. The purpose is to demonstrate an inherent mechanism for metastatic behavior where isolated groups of cancer cells are formed. This parameter vector controls to what extent a more heterogeneous distribution of the growth factor H may occur. In contrast, the parameter vector $\{\lambda_{1i}\}_{i=1}^3$ which effects the production/consumption of chemokine has much less impact on the tumor cells at the tumor margin since cancer cell mobility is directly linked to the fibroblasts, as explicitly expressed through $\hat{\zeta}_c, \hat{k}_c$ and $\hat{\zeta}_{cf}$.

(ii) Second, the possible heterogeneous variation in vascular density and ECM structure, as reflected by the *in vivo* experimental observations in Fig. 2 (A,B,E,F), is accounted for by letting parameters associated with the tissue conductivity and the vascular network vary. Further details follow.

3.3. Intratumoral vascular network, peritumoral lymphatic network, and tissue conductivity

The in silico model (1)–(5) is informed with parameters that characterize the leaky intratumoral vascular network, as expressed through T_v and $\widetilde{P}_v^*$ in (4), the peritumoral lymphatics as expressed through T_l and $\widetilde{P}_l^*$ in (5), and the density of ECM as represented by the hydraulic conductivity of the interstitial space through $\hat{k}_w$ involved in the fluid-ECM interaction term $\hat{\zeta}_w$ in (2). For the filtration coefficients T_v and T_l we use mean values similar to values reported in the literature (Baxter and Jain, 1989; Wu et al., 2013) combined with stochastic-generated variations through a 2D Gaussian variogram constrained such that the resulting IFPs vary within the range reported in Hansem et al. (2019). More precisely, we set maximal intravascular pressure $\widetilde{P}_v^* = 6000$ Pa (45 mmHg) and inner lymphatic pressure $\widetilde{P}_l^* = 600$ Pa (4.5 mmHg). This typically gives a minimum IFP around -2 mmHg in the peritumoral region which is within the range of -3 to $+3$ mmHg assumed for normal tissues (Lunt et al., 2008; Hansem et al., 2019). The other variables $\hat{k}_w, T_v$ and T_l for the case with cervical carcinoma are varied as indicated in Table 3. IFP values are then acquired that are around 10–40 mmHg, as seen in Fig. 2 (C). We note that $\left(I_w \hat{k}_w\right)^{-1}$ amounts to the hydraulic conductivity and takes for the sparse case values in the interval $[1.25 - 5] \cdot 10^{-13}$ (m^2/Pas). This is in the upper range of values used, for example, in Baxter and Jain (1989) and Wu et al. (2013) which vary from $0.64 \cdot 10^{-14}$ till $0.31 \cdot 10^{-13}$

(m^2/Pas). On the other hand, in the case with dense ECM, $\left(I_w \hat{k}_w\right)^{-1}$ varies in the interval $[3.3 - 10] \cdot 10^{-14}$ (m^2/Pas), see Table 4. Moreover, $T_v T^*$ varies within $[0.1 - 4] \cdot 10^{-3}$ (1/Pa) for the sparse case which is comparable to values used by others, e.g., Baxter and Jain (1989) and Wu et al. (2013) where $T_v T^* = 4.2 \cdot 10^{-3}$ (1/Pa). Slightly lower values are used for the dense case (Table 4).

### 3.4. In silico tumor representing cervical carcinoma with homogeneous/compartmentalized ECM

We consider an ensemble composed of 50 realizations of $\hat{k}_w, T_v$, and T_l within the range as specified in Table 3 (sparse) to mimic the situation shown in Fig. 2 (panel A and E) with homogeneous ECM and Table 3 (compartments) to mimic the situation shown in Fig. 2 (panel B and F) with compartments. We represent the tumor histology in Fig. 2 E and F through our parameter that accounts for the resistance to fluid flow, $\hat{k}_w$. The experimental case with homogeneous ECM is translated into a uniform $\hat{k}_w$ (panel G), whereas the compartment case is represented by high value $\hat{k}_w$ bands (panel H). The spatial distribution related to T_v has a Gaussian variogram with practical range of 30 voxels in x and y direction. $T_v T^*$ (where T^* is the reference time, see Table 5 in Appendix A) has a standard deviation of $0.5 \cdot 10^{-3}$ and a mean value of $2 \cdot 10^{-3}$. Meanwhile, the spatial distribution of $T_l T^*$ has a Gaussian variogram with practical range of 2 voxels in x and y direction. Each tumor has a different standard deviation and mean value, ranging from $10^{-4} - 10^{-3}$ and $5 \cdot 10^{-5} - 5 \cdot 10^{-4}$ for the standard deviation and mean value, respectively. See Fig. 3(B) for a typical example.

The distribution of the corresponding different IFPs, as generated by the in silico model and evaluated at two different, fixed positions in the intratumoral region, is shown in Fig. 2 (panel C). We use the notation "ventral" IFP and "dorsal" IFP which refer to two fixed positions in the 2D domain, respectively, corresponding to the grid box $(29, 29)$ and grid box $(33, 33)$ on a grid of 61×61 grid blocks. This mimics what was done in Hansem et al. (2019) where IFP was measured at two different positions. Comparison with Fig. 2 (panel A) reveals that the in silico cervical model largely behaves similarly to the *in vivo* result (Hansem et al., 2019) showing a homogeneous intratumoral IFP. Moreover, for the compartment case shown in Fig. 2 (panel D) the resulting IFP distribution is much more heterogeneous, similar to the experimental results in Fig. 2 (panel B). As seen from Table 3, the main difference between the two cases is that $\hat{k}_w$ for homogeneous ECM can vary within a small interval whereas for the case with arbitrary, high-resistant bands $\hat{k}_w$ will take a very high value where the bands are located. Next, we want to illustrate more details by exploring one of the in silico models shown in Fig. 2, first for the case with homogenous ECM (panel C), then for the case with compartments (panel D). We use one of the high pressure tumors found in Fig. 2 (C) as our homogeneous case, without any other preferences than the high pressure. The corresponding tumor with compartments, which has the same parameters except for the inverse tissue resistance $\hat{k}_w$, is also used.

3.4.1. Homogeneous ECM, high maximal IFP

For this instance we find that the maximal IFP is around 29 mmHg whereas the "measured" dorsal pressure is 27 mmHg and ventral pressure is 28 mmHg. The simulated growth of this in silico model is then computed up to $T = 50$ (around 5.8 days). In Fig. 3 is an illustration of T_v (panel A), and T_l (panel B). Heterogeneity is seen both for T_v and T_l. Moreover, in Fig. 4 the resulting interstitial
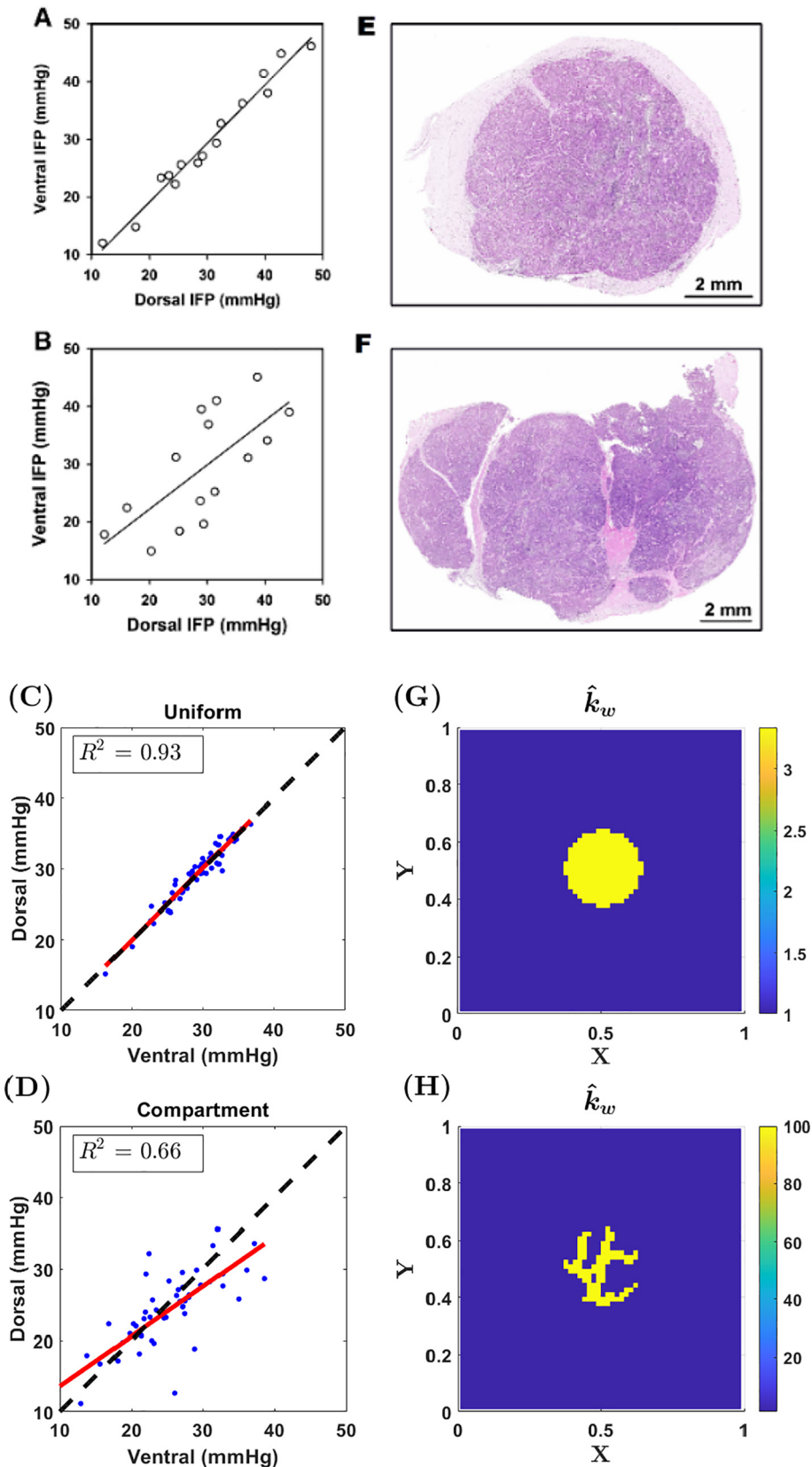
Fig. 2. HL-16 cervical carcinom. Experimental results for (i) homogeneous ECM (A, E); (ii) ECM with compartments (B, F). **A, B** IFP measured at two different locations within a tumor for a total of 15 tumors in both **A** and **B**, for homogeneous ECM seen in **E** and ECM with compartments seen in **F**, respectively. The coefficient of determination for the two plots in **A** and **B** is $R^2 = 0.97$ and $R^2 = 0.49$ respectively. IFP measurements at two locations using 50 simulated tumors are shown in **C** and **D**, with corresponding example tumors seen in **G** and **H**, which are considered representative for **E** and **F**. Panels **(A)**, **(B)**, **(E)** and **(F)** were reproduced from Hansem et al. (2019) [DOI: 10.1016/j.tranon.2019.05.012].

Table 3
Parameters characterizing the TME of cervical carcinoma.

Case	Variable	Description	Values
Sparse	$\hat{k}_w$	fluid-ECM resistance force	$[1-4]$ (*)
	$T_v T^*$	effective vasculature conductivity	$1 \cdot 10^{-4} - 4 \cdot 10^{-3}$ (1/Pa) (**)
	$T_l T^*$	effective lymphatic conductivity	$1 \cdot 10^{-4} - 2 \cdot 10^{-3}$ (1/Pa)
Compartments	$\hat{k}_w$	fluid-ECM resistance force	$\{1, 100\}$
	$T_v T^*$	effective vasculature conductivity	$1 \cdot 10^{-4} - 4 \cdot 10^{-3}$ (1/Pa)
	$T_l T^*$	effective lymphatic conductivity	$1 \cdot 10^{-4} - 2 \cdot 10^{-3}$ (1/Pa)
(*)	$\left(I_w \hat{k}_w\right)^{-1}$	hydraulic conductivity	$[1.25 - 5] \cdot 10^{-13}$ (m²/Pas)
(**)	$T_v = L_v \frac{S_v}{V}$	$L_v = 2.8 \cdot 10^{-7}$ (cm/mmHgs)	$4.2 \cdot 10^{-7}$ (1/Pas)
		$\frac{S_v}{V} = 200$ (cm⁻¹)	(reference (Baxter and Jain, 1989; Wu et al., 2013))

Table 4
Parameters characterizing the TME of pancreatic carcinoma.

| Case	Variable	Description	Value
Sparse	$\hat{k}_w$	fluid-ECM resistance force	$1-4$
	$T_v T^*$	effective vasculature conductivity	$1 \cdot 10^{-4} - 4 \cdot 10^{-3}$ (1/Pa)
	$T_l T^*$	effective lymphatic conductivity	$1 \cdot 10^{-4} - 2 \cdot 10^{-3}$ (1/Pa)
Dense	$\hat{k}_w$	fluid-ECM resistance force	$5-15$ (*)
	$T_v T^*$	effective vasculature conductivity	$1 \cdot 10^{-4} - 1.5 \cdot 10^{-3}$ (1/Pa)
	$T_l T^*$	effective lymphatic conductivity	$1 \cdot 10^{-4} - 2 \cdot 10^{-3}$ (1/Pa)
(*)	$\left(I_w \hat{k}_w\right)^{-1}$	hydraulic conductivity	$[3.3 - 10] \cdot 10^{-14}$ (m²/Pas)
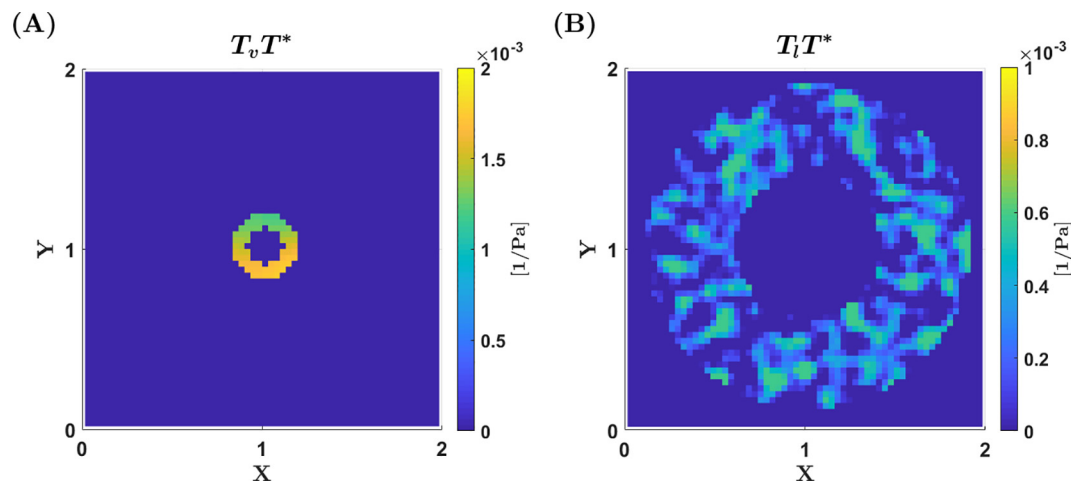
Fig. 3. Parameters characterizing the vascular and lymphatic system, homogenous ECM: **(A)** Vascular filtration constant T_v. The vascular system is placed at the periphery of the primary tumor. **(B)** Lymphatic filtration constant T_l where the lymphatic network is placed in the peritumoral region. The vascular and lymphatic field are both generated through a Gaussian variogram, creating random fields. The filtration constants are multiplied by T^* to yield the unit [1/Pa].

fluid pressure (IFP) P_w is shown in panel A whereas the fluid velocity field $\mathbf{u}_w$ is illustrated in panel B. In particular, we observe that the heterogeneity associated with the leaky vascular system through T_v does not lead to heterogeneous IFP. In panel C and D the corresponding invasive tumor cell and fibroblast behavior are illustrated. Cancer cells (panel C) are themselves fairly immobile due to the high cell-ECM resistance force through the parameter I_c, see Table 7 (Appendix A). Yet, when following fibroblasts (panel D) through direct attachment and/or created tracks they become much more mobile. A strong core of cancer cells remains, as shown in panel C. There are, however, cancer cells following fibroblasts and therefore migrate in sheets away from the primary tumor with

some tendency to create strands and islands. Considering the chemical concentration profiles, panel E (chemokine) and panel F (TGF), positive chemical gradients are formed in the vicinity of the lymphatic network which trigger fibroblasts and cancer cells to move outwardly from the primary tumor.

The migration pattern seen in Fig. 4 does not fully explain the possible metastatic behavior where groups of tumor cells are able to detach from the primary tumor.

As an illustration of the potential aggressive behavior involved in the cell-fibroblast interaction, we modify the parameters $\{\lambda_{2i}\}_{i=1}^5$ involved in $(1)_8$ to give a more heterogeneous distribution of the growth factor H. This, will in turn make the migration of
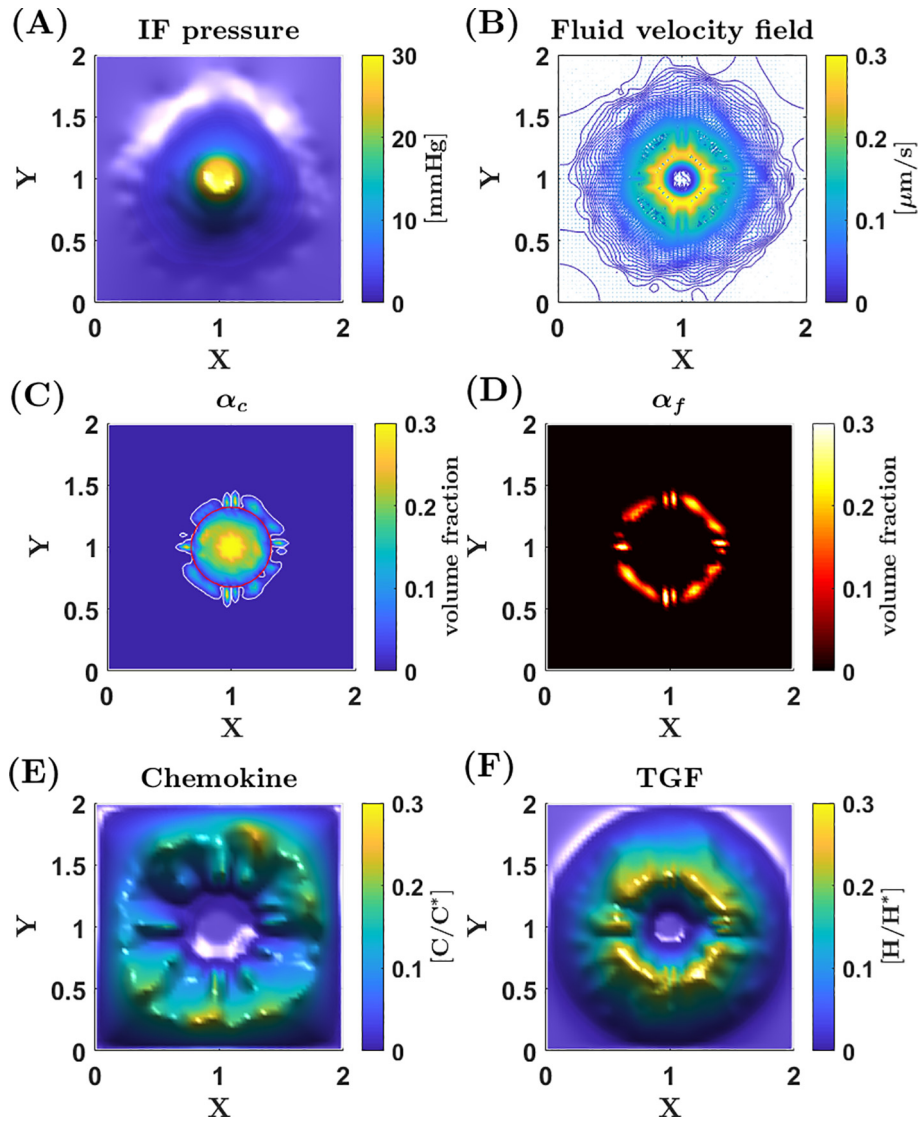
Fig. 4. Simulation results, homogenous ECM: (A) Interstitial fluid pressure in mmHg. The pressure is largest within the tumor due to the leaky vascular system, and decreases quickly at its margin. (B) Fluid velocity field. The fluid originates from the primary tumor and is flowing towards the lymphatics. The effectiveness of the collecting peritumoral lymphatics determines how far the fluid will flow out from the tumor margin. (C) Tumor cell volume fraction at the end of the simulation. The invasive front is fairly regular. The red circle shows the initial tumor cell volume $\alpha_c = 0.01$. The white line is also tumor cell volume fraction $\alpha_c = 0.01$, illustrating the invasive front after simulated period. (D) Fibroblast volume fraction at the end of simulation. The fibroblasts have not migrated far from their initial position seen in Fig. 1 (B). (E) Distribution of chemokine, which is secreted by the tumor cells, is transported through the pore space and is causing tumor cell chemotaxis towards the lymphatics. (F) TGF is produced by fibroblasts and is transported through the pore space. Fibroblasts chemotact towards positive gradients in TGF.

fibroblasts more heterogeneous and invasive. We now use $\lambda_2 = \left(4 \cdot 10^{-7}, 2 \cdot 10^{-7}, 4 \cdot 10^{-7}, 4 \cdot 10^{-10}, 2 \cdot 10^{-5}\right)$, see Table 8 (Appendix A) for comparison with default values. Both the level of production and consumption of the growth factor are reduced. The result is shown in Fig. 5. The change in migration pattern is striking: isolated groups of fibroblasts have formed (panel B) with corresponding isolated islands of tumor cells as well as strands of infiltrating tumor cells (panel A). If we were to consider a tumor with homogeneous histology having low maximal IFP, we generally see less heterogeneous invasion into the tissue compared to Fig. 4C (data not shown). How far into the tissue the tumor cells invade does not change when the IFP is reduced, yet the results show different tumor cell distribution at the invasive front.

### 3.4.2. Compartmentalized ECM, high maximal IFP

We use T_l as for the homogeneous case discussed above but now ECM contains compartments which affect T_v. In Fig. 6 is an

illustration of T_v (panel A) and T_l (panel B). $\hat{k}_w$ is as shown in Fig. 2 (H) and reflects the compartmentalized ECM structure which bears similarity to what is seen experimentally in Fig. 2 (panel E). The simulated progression of the corresponding in silico model is then computed up to $T = 50$ (around 5.8 days). The resulting two "measured" IFPs are, respectively, 26 and 29 mmHg, while the maximal IFP is closer to 31 mmHg. In Fig. 7 the resulting interstitial fluid pressure (IFP) P_w is shown in panel A whereas the fluid velocity field $\mathbf{u}_w$ is illustrated in panel B. We observe that a considerably more heterogeneous IFP is generated within the tumor as compared to Fig. 4A. Other observations are:

- We have assumed the same distribution of the peritumoral lymphatics through T_l as before, see Fig. 6B. However, the vascular distribution through T_v, (A), is now dependent on the location of thick ECM bands, causing low fluid production from the vessels within the bands.
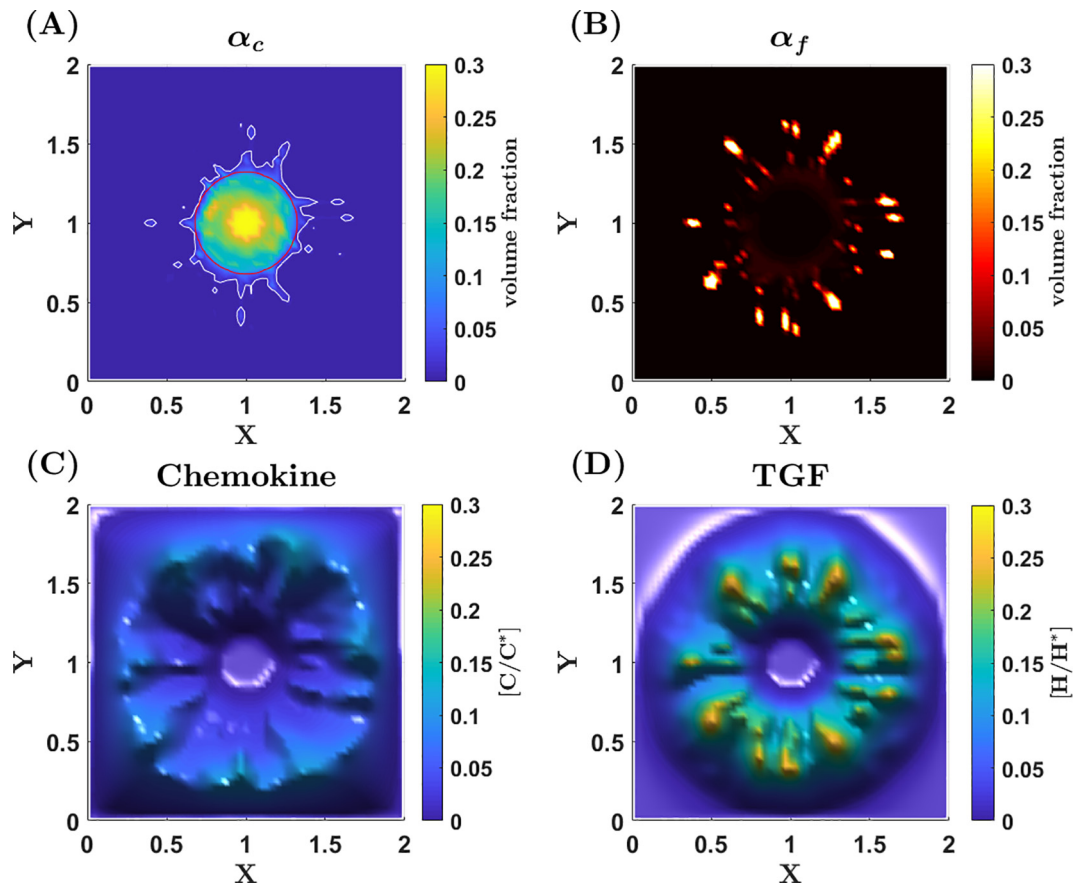
Fig. 5. Increased aggressiveness, homogeneous ECM: The production/consumption of TGF is now altered to yield a more heterogeneous distribution in the tissue. **(A)** Cancer cell volume fraction. Compared to the case in Fig. 4 (C), the tumor cells invade further into the normal tissue while also acting more heterogeneous. **(B)** Fibroblast volume fraction. The fibroblasts play an important role in causing tumor cell migration to be more aggressive. **(C)** Chemokine concentration C shows a similar pattern as in Fig. 4 but with a lower concentration (E). **(D)** Transforming growth factor concentration, H, is now much more heterogeneous, which causes the fibroblasts to chemotact in different directions and in terms of isolated groups.
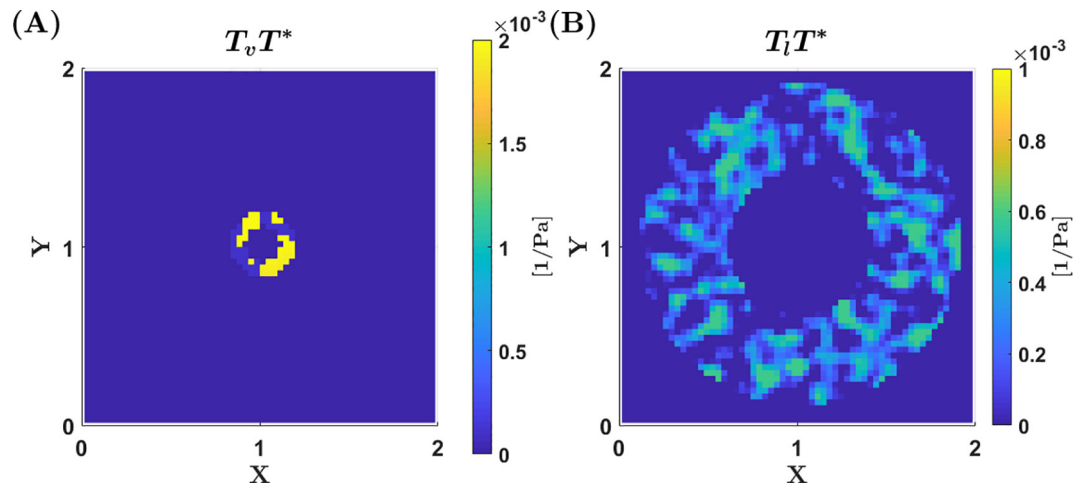
Fig. 6. Parameters characterizing the vessel system, compartmentalized ECM: (A) Vascular filtration constant T_v. The ECM bands affect the filtration constant T_v, decreasing it to very low values within the bands. **(B)** Lymphatic filtration constant T_l is the same as for the homogenenous case, seen in Fig. 3 (B).

- The tumor cell migration behavior seen in Fig. 7C largely is a result of the CAFs migration behavior, as reflected in Fig. 7D. The invasion front is quite heterogeneous. In the north-west direction an isolated island of tumor cells have evolved. The dis-

tribution of chemokine and TGF (which play a role in the chemotaxis of tumor cells and CAFs, respectively) is shown in panel E and F. The distribution is largely a result of the IF velocity field shown in Fig. 7B. The simulation suggests that the more
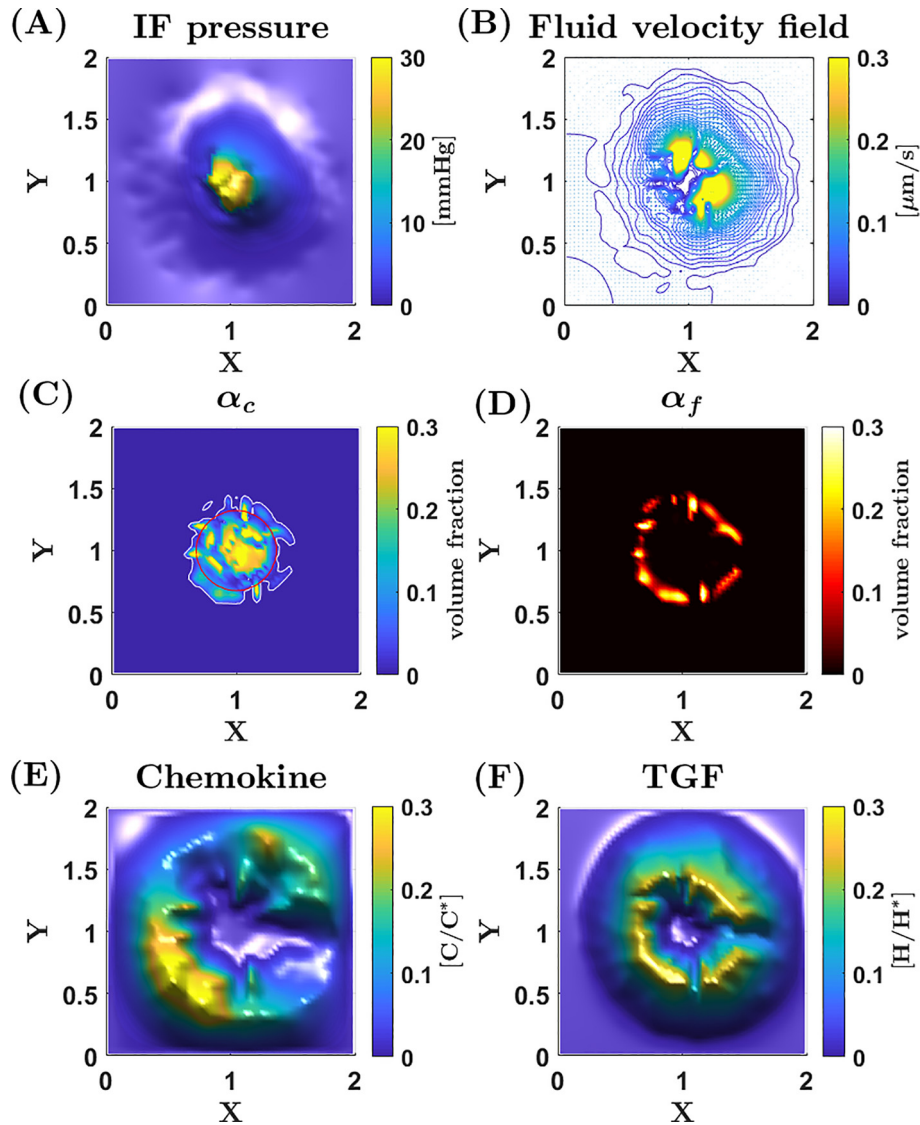
Fig. 7. Simulation results, compartmentalized ECM: **(A)** Interstitial fluid pressure in mmHg. The IFP is highly heterogeneous throughout the tumor due to the compartments. The compartments have the effect of preventing the IFP to even itself out within the tumor. **(B)** Interstitial fluid velocity which correlates with the ECM structure and IFP distribution. Since the pressure is quite heterogeneous with locally elevated pressures caused by ECM bands with very high resistance to fluid flow, the fluid velocity field also becomes heterogeneous. There are peaks in fluid velocity where fluid may exit the tumor and is not blocked by the ECM bands seen in Fig. 2 (H). **(C)** Tumor cell volume fraction at the end of the simulation. At the upper part of the tumor it is evident that some tumor cells have formed an isolated island. Invasive fingers are about to evolve to the right. **(D)** Fibroblast volume fraction distribution is fairly heterogeneous in its invasion into the tissue and correlates with the distribution of TGF. **(E)** The chemokine distribution is a result of the heterogeneous IF velocity field. Higher concentrations are seen in regions where flow velocity is low. **(F)** TGF shows a heterogeneous distribution which correlates to the IF velocity field. This causes a more heterogeneous migration pattern of the fibroblasts which is transmitted to cancer cells in contact with fibroblasts.

heterogeneous distribution of the TGF growth factor H due to the presence of the different compartments has triggered this metastatic behavior.

- We increase the heterogeneity in growth factor distribution by changing $\{\lambda_{2i}\}$ as for the previous case. The resulting behavior of the in silico model is shown in Fig. 8. Again, we see that the collective outgoing groups of CAFs (panel B) trigger a more aggressive tumor cell migration behavior resulting in strands and islands (panel A).

If we were to use a case with low maximum IFP, we typically see less heterogeneous invasion into the tissue. The low IFP causes less room for heterogeneous pressure between the different compartments and therefore the tumor migration is also less heterogeneous.

3.5. In silico tumor representing pancreatic carcinoma with sparse/dense ECM

Now we focus on the experimental findings for pancreatic cancer reported in Hansem et al. (2019). The situation shown in Fig. 9 (panel A and E) for Panc-1 pancreatic carcinoma xenograft model with sparse ECM bears similarities to the case with HL-16 cervical carcinoma with homogenous ECM, which was explored above. In particular, the simulations carried out for that case seem representative for the case with pancreatic cancer with sparse ECM with input parameters for $\hat{k}_w$, T_v, and T_l as indicated in Table 4. Hence, we focus on the case with dense ECM. The dense ECM is accounted for by letting the resistance force through $\hat{k}_w$ vary within a larger interval and with higher values but such that it takes a constant value for each in silico tumor. At the same time we assume that
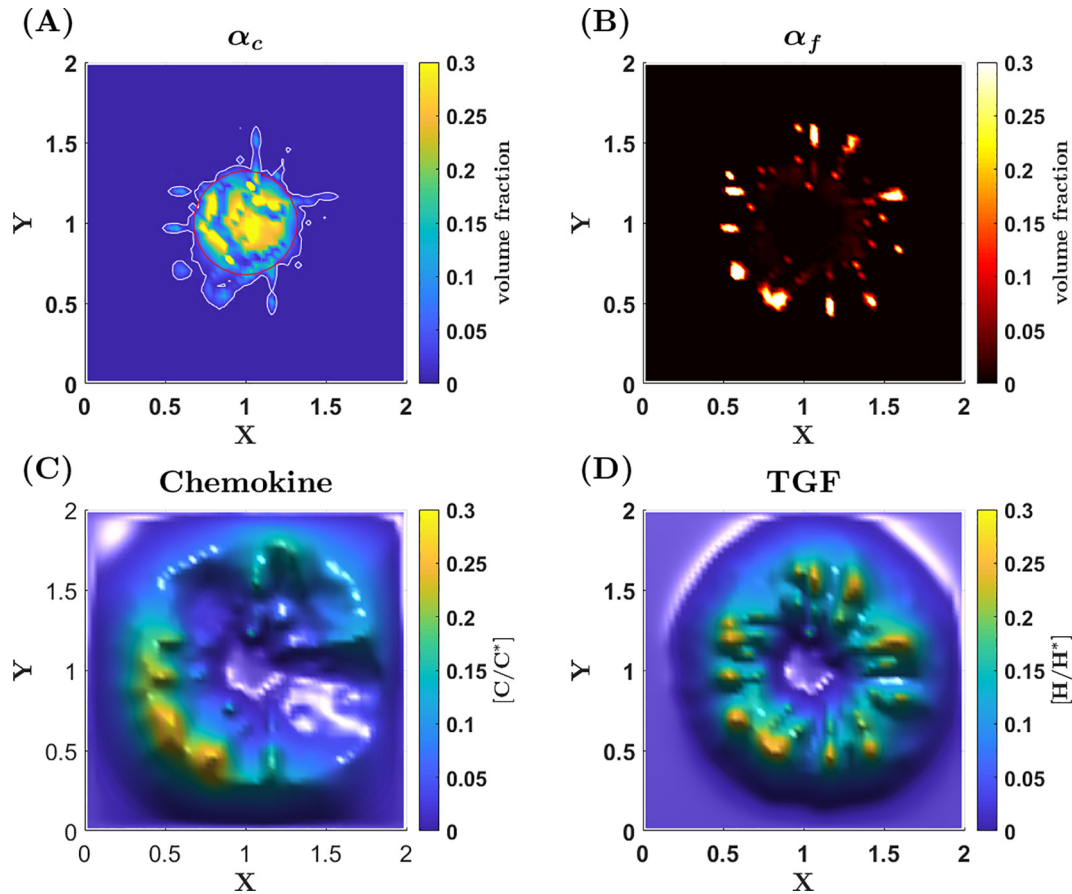
Fig. 8. Increased aggressiveness, compartmentalized ECM. **(A)** Tumor cell volume fraction distribution now has several fingers migrating out from the primary tumor and several isolated islands, as compared to the previous case seen in Fig. 7 (C). **(B)** Fibroblasts are migrating in groups towards the lymphatics, causing the fingering effect seen in (A). **(C)** Chemokine concentration C is similar to the previous cases. **(D)** Transforming growth factor concentration H correlates to fibroblast concentration seen in (B). The chemical distribution is heterogeneous and has positive gradients in the direction of the lymphatics.

this denser, desmoplastic ECM increases the collapse of leaky vascular vessels giving rise to a lower value of T_v, as reflected by the interval given in Table 4 (dense). This also ensures that the resulting IFP values remain within a pathological reasonable range. We assume that the lymphatic network is characterized as before. Again, an ensemble of 50 in silico pancreatic tumors are generated. The corresponding IFP at the two different positions (ventral and dorsal) are recorded and plotted in Fig. 9 (panel D). Analogous to Fig. 2 the ventral IFP and dorsal IFP seen on the axes describe that the measurements are performed at two different positions corresponding to grid box $(29, 29)$ and grid box $(33, 33)$ on a grid of 61×61 grid blocks. Similar to the experimental results shown in Fig. 9 (panel B), the resulting IFP shows a heterogeneous distribution. In the following, we take a closer look at possible mechanisms behind this heterogeneous intratumoral IFP.

3.5.1. Dense ECM, high maximal IFP

We choose a member from the stochastic generated ensemble different from the one used for homogeneous HL-16 cervical with respect to T_v and T_l distribution as well as the initial fibroblast distribution. Then we simulate tumor progression for a time period of $T = 50$ (5.8 days). The results are shown in Fig. 10–12. Some essential points are:

- The heterogeneity in the microvascular network through T_v is seen in Fig. 10 (panel A) as well as for T_l (panel B). The dense ECM is reflected by a high value of $\hat{k}_w$ around 12 as seen in Fig. 9 (panel H). Corresponding to this characterization of

TME, the resulting IFP shown in Fig. 11 (panel A) is high (maximum around 35 mmHg) and heterogeneous within the tumor. The dorsal and ventral IFP take the values 26 and 31, respectively.

- The tumor cell migration behavior is seen in Fig. 11 (panel C) and is largely a result of the fibroblast migration behavior seen in panel D. The invasive front is fairly regular with no indication of metastatic propensity. This is naturally linked to the relatively homogeneous distribution of chemokine (panel E) and TGF growth factor (panel F). However, we may allow the distribution of the TGF factor H becoming more heterogeneous (as a result of the heterogenous T_l) by modifying the values of the rate coefficients represented by $\{\lambda_{2i}\}$ involved in the transport-reaction equation for H in $(1)_8$. We modify $\{\lambda_{2i}\}$ as we did for the in silico cervical model. Fig. 12 (panel A) shows how the cell-fibroblast interaction now results in formation of many isolated islands, a behavior which is natural to link to high metastatic propensity. This is a consequence of the heterogeneous distribution of TGF (panel D) and the resulting heterogeneous distribution of fibroblasts (panel B).

4. Discussion

4.1. Conclusions

The in silico cervical cancer model has demonstrated that homogeneous and sparse ECM was associated with a relatively constant (uniform) intratumoral IFP. This was observed despite
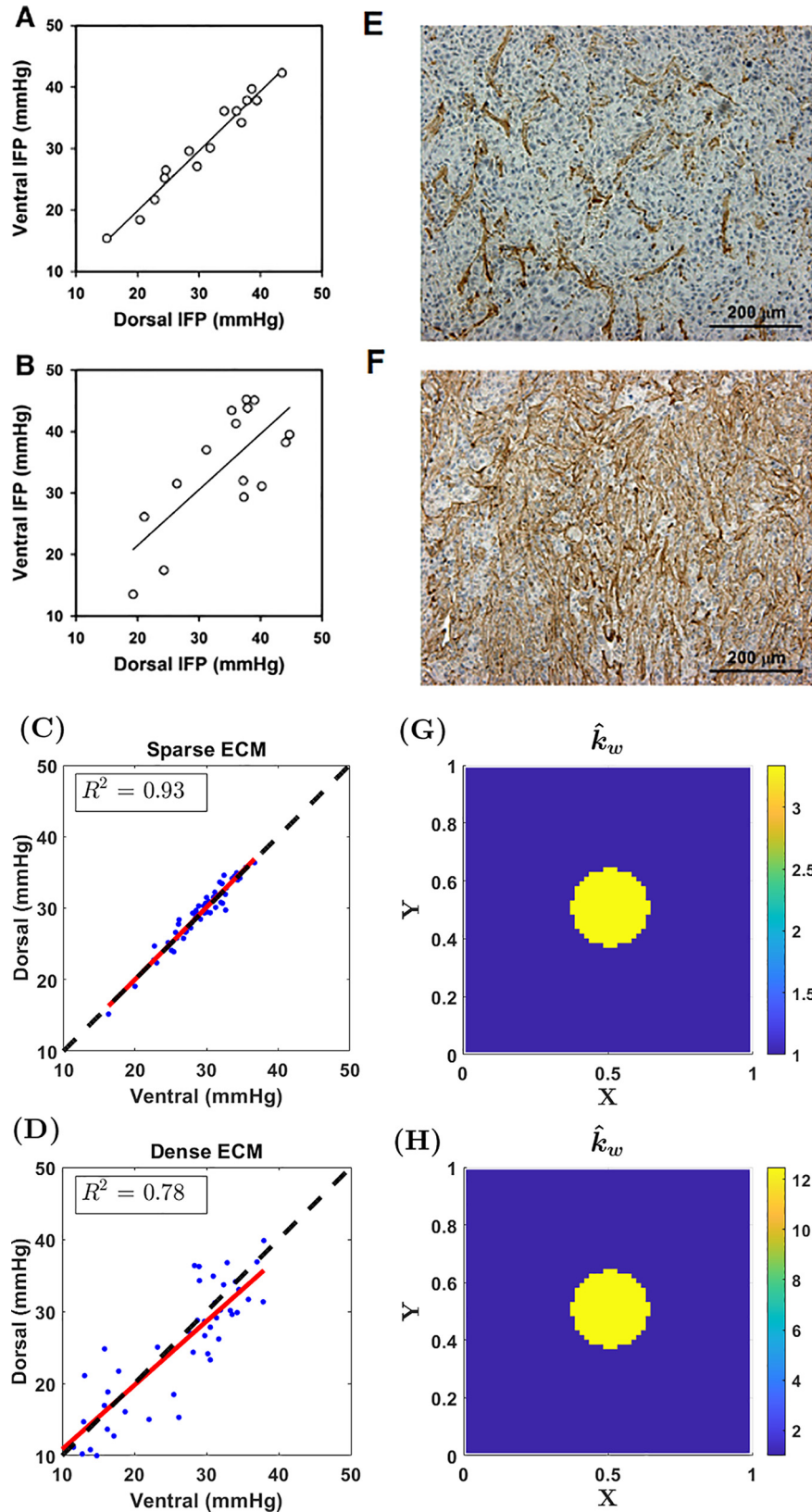
Fig. 9. Panc-1 pancreatic carcinoma. Experimental results for (i) sparse ECM (A, E); (ii) dense ECM (B,F). **A, B** IFP measurements taken at two different places within a tumor for a total of 15 of each type of histology, corresponding to **E** and **F**. The respective coefficient of determination for **A** and **B** are $R^2 = 0.96$ and $R^2 = 0.54$. The computational model uses 50 tumors of each type of histology to plot the two IFP measurements in **C** and **D**. Within each plot the R^2 value is shown. The corresponding histology is represented by $\hat{k}_w$ in **G** and **H**. Panels **(A)**, **(B)**, **(E)** and **(F)** were reproduced from Hansem et al. (2019) [DOI: 10.1016/j.tranon.2019.05.012].
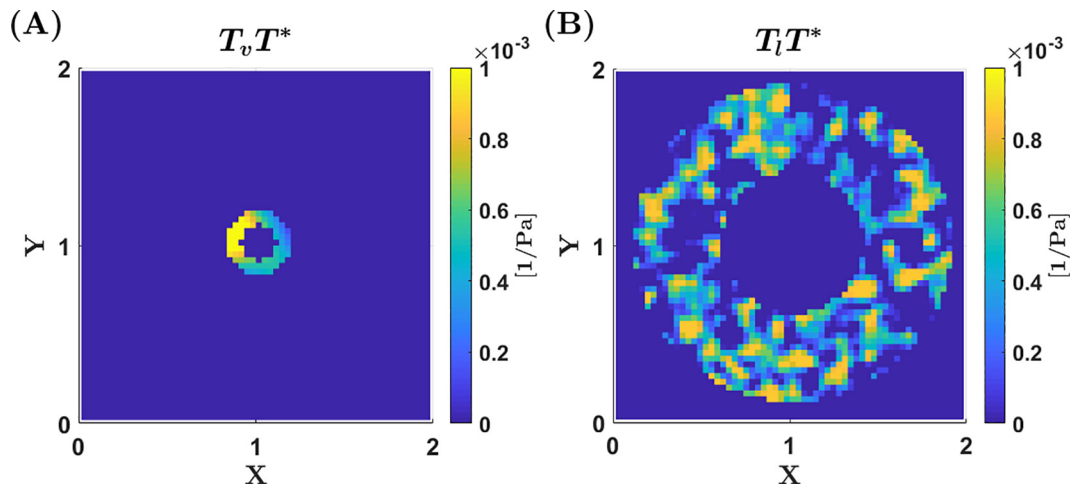
Fig. 10. Parameters characterizing the vascular and lymphatic system, dense ECM: **(A)** The vascular filtration constant T_v that determines the fluid production from the blood vessels within the tumor. **(B)** T_l characterizing the lymphatic network, which is placed in the area surrounding the primary tumor. The values of both T_v and T_l are generated through a Gaussian variogram, while the placement of the vessels is constant.

the fact that a heterogeneous microvascular network, possibly as a result of heterogeneous accumulation of solid stress owing to tumor growth (Mpekris et al., 2015; Jain et al., 2014), was assumed by generating T_v as a 2D Gaussian variogram and constrained such that the resulting IFP varied in the relevant range 10–45 mmHg. Inclusion of compartments separated with high-resistant bands was associated with heterogeneous intratumoral IFP when the heterogeneous T_v was generated similar to the case with homogeneous ECM structure. This confirms the underlying hypothesis suggested in Hansem et al. (2019) that structures within the ECM that prevent fluid flow can explain the heterogeneous IFP observed for HL-16 cervical carcinoma.

For pancreatic cancer the in silico model demonstrated that dense ECM structure (but homogeneous) combined with heterogeneous microvascular density through the randomly generated T_v typically gave rise to a heterogeneous intratumoral IFP. The dense ECM structure, as reflected by a high resistance force to fluid flow through a uniform but high $\hat{k}_w$, implies that the heterogeneity in T_v is translated into a heterogeneous IFP. In conclusion, the in silico model confirms that tissue stromal elements represented a barrier against interstitial convection, thus preventing local differences in IFP from being leveled out by intratumoral fluid flow for the case with Panc-1 pancreatic carcinoma (Hansem et al., 2019).

By varying the parameters $\{\lambda_{2i}\}$ that regulate the production/-consumption of TGF, a more heterogeneous distribution was achieved which gave rise to more aggressive behavior, both for tumor cells and fibroblasts (Figs. 5, 8,12). These figures are included in order to illustrate that the in silico model is able to yield a variety of results depending on the set parameters. It is also important to note, that this attribute of the model could be used in the manner of tuning parameters to better comply with an individual tumor where more specific information is available (Hormuth et al., 2019; Jarrett et al., 2018). For instance, in our simulations we have assumed that the characteristics with regard to the cell-substrate resistance force, cell–cell adhesion, chemotaxis coefficients and so on, are the same for both tumor types. While this is a clean way of performing simulations, it is not necessarily true and one could envision to use different sets of parameters for the two tumors.

The proposed in silico model, previously explored and tested in Urdal et al. (2019) and Waldeland et al. (2020), accounts for fluid-sensitive migration mechanisms found from *in vitro* studies (Shieh et al., 2011; Polacheck et al., 2011) which involve autologous chemotaxis related to cancer cells and fibroblasts, combined with

ECM remodelling and cell-fibroblast interaction. The combination of the leaky intratumoral vascular network and the peritumoral lymphatic network which collects this fluid gives rise to elevated IFP. This situation might be associated with high metastatic propensity because hem- and lymphangiogenic factors, proteolytic enzymes, cytokines, and other metastasis-promoting molecules are transported from the primary tumor into peritumoral lymphatics (Wiig and Swartz, 2012; Hansem et al., 2019). The in silico model has demonstrated that when tumor cells are armed with these mechanisms, the progression of the tumor can result in aggressive behavior where groups of tumor cells detach from the primary tumor and form isolated islands. It is natural to link this behavior to increased metastatic propensity. In fact, the study in Onozato et al. (2013), though in the context of lung cancer, found a direct association between formation of isolated islands composed of groups of tumor cells and metastatic propensity. The prognosis of lung adenocarcinomas with tumor islands was significantly worse than those without. The in silico model suggests that the combination of heterogeneous fibroblast migration and cell-fibroblast interaction can be a driver for this aggressive behavior. The findings in Hansem et al. (2019) have suggested that the common assumption that resistance to interstitial fluid flow is low in tumor tissue is not necessarily valid for tumors developing a complex, dense, and heterogeneous stroma. The suggested in silico model has more precisely illustrated the mechanisms that most likely are at play. In particular, it has demonstrated how barriers against interstitial convection may have significant implications for the distribution of all kinds soluble molecules produced and secreted by cancer and stromal cells. This also will carry over to the distribution of chemical therapeutic agents. The computer model therefore can be interesting to use to explore barriers for efficient delivery of therapeutic drugs.

4.2. Limitations of the model

A limitation of the current version of the in silico model is that it does not explain the reported correlation that seems to exist between high IFP and high metastatic propensity, as found in Hansem et al. (2019), Andersen et al. (2017) and related work Hompland et al. (2012). Presuming that isolated islands is a means to metastasis, the model does not indicate that a tumor case with high IFP tends to be more metastatic. Both high IFP tumors and low IFP tumors show a similar tendency to generate isolated islands. More precisely, this behavior seems to depend more strongly on
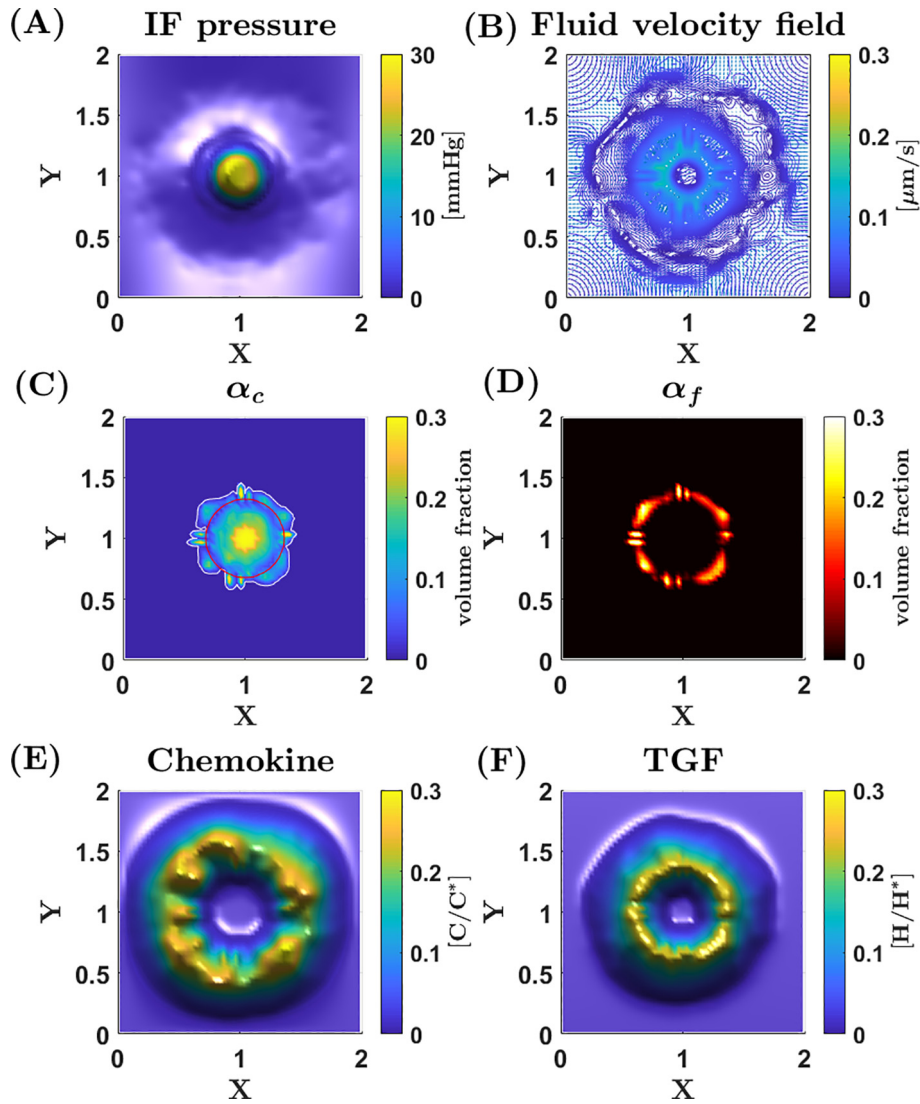
Fig. 11. **Simulation results, dense ECM**: **(A)** The resulting IFP is clearly correlated to the vascular filtration constant T_v shown in Fig. 10A. The resistance to fluid flow within the tumor is high (high $\hat{k}_w$ value), which causes the pressure not to be evened out, leading to heterogeneous IFP. **(B)** Interstitial fluid velocity is low for this type of histology, even though it has a similar magnitude in IFP as for previous cases. This is caused by the high resistsance to fluid flow within the tumor, leading to a lower exit velocity of the fluid. **(C)** The tumor cell volume fraction is fairly homogeneous and the invasion is quite limited. **(D)** Fibroblasts show little aggressive behavior and have not migrated far from their initial position. **(E)** Due to the low fluid velocity, chemokine concentration in peritumoral region is higher than for the case with sparse ECM in Fig. 4. **(F)** TGF distribution.

a heterogeneous distribution of the TGF concentration H than on the level of IFP. In fact, we found that the parameter family $\{\lambda_{2i}\}$ in $(1)_8$ which controls the production, consumption and decay of TGF, largely affected the level of heterogenity in TGF distribution in the peritumoral region. Apparently, the mathematical model lacks some sort of aggressiveness when it comes to fluid-sensitive migration mechanisms. However, it has been observed (Waldeland and Evje, 2018; Evje and Waldeland, 2019) that mathematical models which include the combination of downstream migration driven by autologous chemotaxis and strain-induced upstream mechanisms (Follain et al., 2020; Polacheck et al., 2011; Polacheck et al., 2014) suggest that aggressive tumor cell behavior is correlated to higher IFP. An interesting extension of the mathematical model discussed in the current work would be to account for such mechanisms.

The multiphase model explored in this work has been designed to capture bulk-level aspects of tumor growth and metastatic propensity when constrained by data from the study of preclinical models in Hansem et al. (2019). In that sense the model bears sim-

ilarities to the mathematical models explored in Weis et al. (2015) and Weis et al. (2017) which focus on capturing first-order effects pertaining to tumor progression and avoid representing many different parameters which are impractical or impossible to measure clinically. Extended computer models may also involve a multi-scale approach where one can explore tumor growth by considering major biological events at both tissue, cellular, and subcellular scale (Rahman et al., 2017). This has been outside the scope of the current investigations. Finally, in light of the works (Breward et al., 2002; Byrne et al., 2003; Hubbard and Byrne, 2013; Wu et al., 2013; Wu et al., 2014; Mascheroni et al., 2016; Mascheroni et al., 2017; d'Esposito et al., 2018; Lewin et al., 2020; Mpekris et al., 2015; Angeli and Stylianopoulos, 2016; Weis et al., 2015; Jarrett et al., 2018; Hormuth et al., 2019) mentioned in the introduction, there is certainly room for improvements of the current version of the model by including other effects relevant for tumor progression that currently are ignored. However, such extensions might be guided by a concrete need to use the model to explain certain experimental findings.
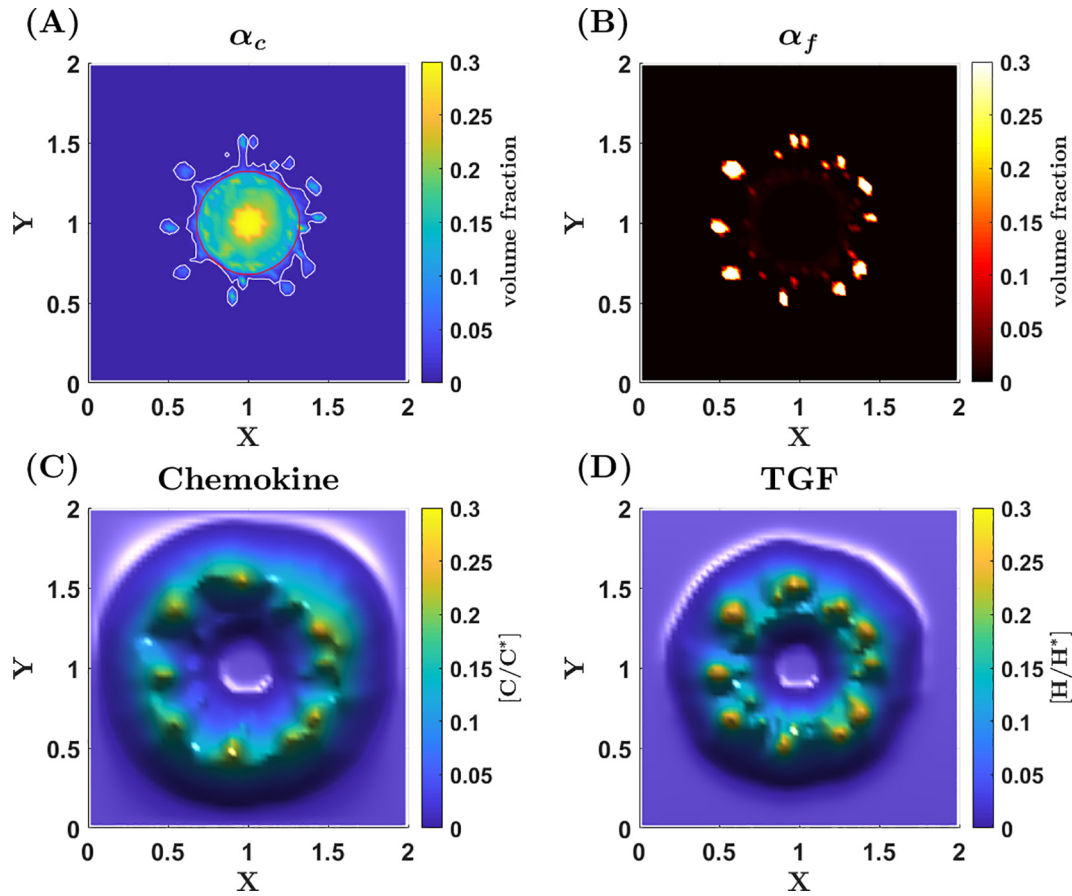
Fig. 12. **Increased aggressiveness, dense ECM.** **(A)** The cancer cells now invade much further into the surrounding tissue, leading to both isolated islands and fingering. **(B)** Fibroblasts migrate in small clusters outwards from the primary tumor, thereby guiding groups of cancer cells effectively away from the primary tumor. **(C)** The chemokine concentration is heterogeneous in its concentration profile. **(D)** Transforming growth factor concentration H distribution is heterogeneous, causing fibroblasts to move in clusters.

Declaration of Competing Interest

The authors declare that they have no known competing financial interests or personal relationships that could have appeared to influence the work reported in this paper.

Acknowledgement

Appendix A. Input parameters

See Tables 5–8.

Table 5
Reference variables.

Variable	Description	Values
T^*	Reference time	10^4 s
L^*	Reference length	0.01 m
u^*	Reference velocity	10^{-6} m/s
D^*	Reference diffusion	10^{-8} m²/s
P^*	Reference pressure	10^4 Pa
C^*, H^*	Reference chemokine, TGF density	10^{-4} kg/m³
C_M, H_M	Max chemokine, TGF density	$0.3C^*, 0.5H^*$

Appendix B. Discretization of the model

We solve the model (1) subject to the boundary condition (9) and the initial conditions (10). The main steps in the solution approach are as follows: We assume that we have an approximate solution at time level t^n given by $\left(\alpha_c^n, \alpha_f^n, C^n, H^n\right)$. Then, we want to

Table 6
Functions involved in cell migration given by Eqs. (6) and (7) (from Urdal et al. (2019)).

Function		Description	Values
$\Delta P_{cw}(\alpha_c)$	=	$-\gamma_c \ln(\delta_c + [1 - \alpha_c])$	(δ_c=0.01; γ_c=1 kPa)
$\Delta P_{fw}(\alpha_f)$	=	$\gamma_f \alpha_f^{\delta_f}$	(δ_f=10; γ_f=7.5 kPa)
$\Lambda_C(C)$	=	$-\frac{\Lambda_{C1}}{1+\exp(-\xi_C(C-C_M))}$	(Λ_{C1}=25 kPa; $\xi_C = 8/C^*$ m³/kg)
$\Lambda_H(H)$	=	$-\frac{\Lambda_{H1}}{1+\exp(-\xi_H(H-H_M))}$	(Λ_{H1}=50 kPa; $\xi_H = 16/H^*$ m³/kg)
$\hat{f}_c(\alpha_c,\alpha_f)$	=	$\frac{\alpha_c\left[\alpha_f\check{\xi}_{cf}+\alpha_c\left(\check{\xi}_{cf}+\check{\xi}_f\right)\right]}{(\alpha_c+\alpha_f)^2\check{\xi}_{cf}+\alpha_c^2\check{\xi}_f+\alpha_f^2\check{\xi}_c+\frac{\alpha_w^2}{\check{\xi}w}\left(\check{\xi}_c\check{\xi}_{cf}+\check{\xi}_c\check{\xi}_f+\check{\xi}_{cf}\check{\xi}_f\right)}$	(see Eqs. (2) and (3))
$\hat{f}_f(\alpha_c,\alpha_f)$	=	$\frac{\alpha_f\left[\alpha_c\check{\xi}_{cf}+\alpha_f\left(\check{\xi}_{cf}+\check{\xi}_c\right)\right]}{(\alpha_c+\alpha_f)^2\check{\xi}_{cf}+\alpha_c^2\check{\xi}_f+\alpha_f^2\check{\xi}_c+\frac{\alpha_w^2}{\check{\xi}w}\left(\check{\xi}_c\check{\xi}_{cf}+\check{\xi}_c\check{\xi}_f+\check{\xi}_{cf}\check{\xi}_f\right)}$	(see Eqs. (2) and (3))
$\hat{h}_1(\alpha_c,\alpha_f)$	=	$\frac{\alpha_c\frac{\alpha_w^2}{\check{\xi}w}\left[\alpha_c\left(\check{\xi}_f+\check{\xi}_{cf}\right)+\alpha_f\check{\xi}_{cf}\right]\phi}{(\alpha_c+\alpha_f)^2\check{\xi}_{cf}+\alpha_c^2\check{\xi}_f+\alpha_f^2\check{\xi}_c+\frac{\alpha_w^2}{\check{\xi}w}\left(\check{\xi}_c\check{\xi}_{cf}+\check{\xi}_c\check{\xi}_f+\check{\xi}_{cf}\check{\xi}_f\right)}$	(see Eqs. (2) and (3))
$\hat{h}_2(\alpha_c,\alpha_f)$	=	$\frac{\alpha_c\alpha_f\left(\alpha_c\alpha_f-\frac{\alpha_w^2}{\check{\xi}w}\check{\xi}_{cf}\right)\phi}{(\alpha_c+\alpha_f)^2\check{\xi}_{cf}+\alpha_c^2\check{\xi}_f+\alpha_f^2\check{\xi}_c+\frac{\alpha_w^2}{\check{\xi}w}\left(\check{\xi}_c\check{\xi}_{cf}+\check{\xi}_c\check{\xi}_f+\check{\xi}_{cf}\check{\xi}_f\right)}$	(see Eqs. (2) and (3))
$\hat{h}_3(\alpha_c,\alpha_f)$	=	$\frac{\alpha_f\frac{\alpha_w^2}{\check{\xi}w}\left[\alpha_c\check{\xi}_{cf}+\alpha_f\left(\check{\xi}_c+\check{\xi}_{cf}\right)\right]\phi}{(\alpha_c+\alpha_f)^2\check{\xi}_{cf}+\alpha_c^2\check{\xi}_f+\alpha_f^2\check{\xi}_c+\frac{\alpha_w^2}{\check{\xi}w}\left(\check{\xi}_c\check{\xi}_{cf}+\check{\xi}_c\check{\xi}_f+\check{\xi}_{cf}\check{\xi}_f\right)}$	(see Eqs. (2) and (3))

Table 7

Parameters characterizing the mobility of tumor cells and fibroblasts by Eq. (2) (from Urdal et al. (2019)).

Variable	Description	Values
$I_w, \hat{k}_w, r_w$	fluid-ECM interaction	$2 \cdot 10^{12}$ (Pas/m²)(*), 1, 0
I_c, r_c	cell-ECM interaction	$2000 I_w$ (Pas/m²), 0.6
$I_f, \hat{k}_f, r_f$	fibroblast-ECM interaction	$100 I_w$ (Pas/m²), 1, 0.6
I_{cf}, r_{cf}, r_{fc}	cell-fibroblast interaction	$1000 I_w$ (Pas/m²), 0.5, 0.5
$A, B\ (\hat{k}_c)$	Reduced cell-ECM resistance (see Eq. (3))	0.7, 50
(*) I_w^{-1}	hydraulic conductivity reference	$5 \cdot 10^{-13}$ (m²/Pas)
	=	$6.7 \cdot 10^{-7}$ (cm²/mmHgs)

Table 8

Parameters for production/decay of chemical agents by Eqs. (1)$_{7,8}$ (from Urdal et al. (2019))

Variable	Description	Values
D_C	Diffusion coefficient chemokine	14×10^{-12} m²/s
D_H	Diffusion coefficient TGF	8×10^{-12} m²/s
λ_{11}	Proteolytically freed chemokine	5×10^{-3} m³/kgs
λ_{12}	Logistic rate constant chemokine	5×10^{-3} m³/kgs
λ_{13}	Cell consumption rate chemokine	1×10^{-4} 1/s
v_C, M_C	Logistic rate exponent, absorption percentage	$0.25, 50\%$
λ_{21}	Proteolytically freed TGF	1.4×10^{-6} m³/kgs
λ_{22}	Logistic rate constant TGF	4×10^{-6} m³/kgs
λ_{23}	Logistic rate constant TGF	5.5×10^{-7} m³/kgs
λ_{24}	Cell consumption rate TGF	4×10^{-3} 1/s
λ_{25}	Natural decay of TGF	2×10^{-5} 1/s
v_H, M_H	Logistic rate exponent, absorption percentage	$0.2, 50\%$

compute the approximate solution $\left(\alpha_c^{n+1}, \alpha_f^{n+1}, C^{n+1}, H^{n+1}\right)$ at the new time step t^{n+1}:

(i) First, we solve the elliptic, steady-state diffusion problem for the IF pressure P_w^n:

$$\nabla \cdot \left(\hat{\lambda}_T \nabla P_w\right), = -T_v\left(\widetilde{P}_v^* - P_w\right) + T_l\left(P_w - \widetilde{P}_l^*\right)$$
$$-\nabla \cdot \left(\hat{\lambda}_c \nabla (\Delta P_{cw} + \Lambda_C)\right) - \nabla \cdot \left(\hat{\lambda}_f \nabla (\Delta P_{fw} + \Lambda_H)\right)$$
$$P_w|_{\partial\Omega} = P_B^*$$

(11)

(ii) Then we can compute the corresponding total velocity $\mathbf{U}_T^n$ from

$$\mathbf{U}_T = \mathbf{U}_c + \mathbf{U}_f + \mathbf{U}_w = -\hat{\lambda}_T \nabla P_w - \hat{\lambda}_c \nabla (\Delta P_{cw} + \Lambda_C)$$
$$-\hat{\lambda}_f \nabla (\Delta P_{fw} + \Lambda_H),$$

(12)

where $\mathbf{U}_i = \alpha_i \mathbf{u}_i, i = w, c, f$. Hence, we have the information we need to evaulate $\mathbf{u}_c^n, \mathbf{u}_f^n$, and $\mathbf{u}_w^n$ based on (6)–(8).

(iii) Armed with interstitial velocities $\mathbf{u}_c^n$ and $\mathbf{u}_f^n$ at time level t^n, we can compute updated volume fractions α_c^{n+1} and α_f^{n+1} from (1)$_{1,2}$. Moreover, by means of $\mathbf{u}_w^n$ we can compute updated concentrations C^{n+1} and H^{n+1} from (1)$_{7,8}$. We employ standard upwind for spatial discretization of convective terms (explicit in time) whereas diffusion terms are treated implicitly in time.

References

Aanonsen, S.I., Nævdal, G., Oliver, D.S., Reynolds, A.C., Vallès, B., 2009. The ensemble Kalman filter in reservoir engineering – a review. SPE J.

Alert, R., Trepat, X., 2020. Physical models of collective cell migration. Annu. Rev. Condensed Matter Phys. 11, 77–101.

Andersen, L.M.K., Wegner, C.S., Simonsen, T.G., Huang, R., Gaustad, J.-V., Hauge, A., Galappathi, K., Rofstad, E.K., 2017. Lymph node metastasis and the physicochemical micro-environment of pancreatic ductal adenocarcinoma xenografts. Oncotarget 8 (29), 48060.

Angeli, S., Stylianopoulos, T., 2016. Biphasic modeling of brain tumor biomechanics and response to radiation treatment. J. Biomech. 49, 1524–1531.

Barbazán, J., Vignjevic, D.M., 2019. Cancer associated fibroblasts: is the force the path to the dark side? Curr. Opin. Cell Biol. 56, 71–79.

Baxter, L., Jain, R., 1989. Transport of fluid and macro molecules in tumors 1. Role of interstitial pressure and convection. Microvasc. Res. 37 (1), 77–104.

Bijlsma, M.F., van Laarhoven, H.W., 2015. The conflicting roles of tumor stroma in pancreatic cancer and their contribution to the failure of clinical trials: a systematic review and critical appraisal. Cancer Metastasis Rev. 34 (1), 97–114.

Breward, C., Byrne, H., Lewis, C., 2002. A two-phase model of solid tumour growth. J. Math. Biol. 45, 125–152.

Byrne, H., Preziosi, L., 2003. A two-phase model of solid tumour growth. Math. Med. Biol. 20, 341–366.

Byrne, H., King, J., McElwain, D., Preziosi, L., 2003. A two-phase model of solid tumour growth. Appl. Math. Lett. 16, 567–573.

Castellanos, E., Berlin, J., Cardin, D.B., 2011. Current treatment options for pancreatic carcinoma. Curr. Oncol. Rep. 13 (3), 195–205.

Chauhan, V.P., Boucher, Y., Ferrone, C.R., Roberge, S., Martin, J.D., Stylianopoulos, T., Bardeesy, N., DePinho, R.A., Padera, T.P., Munn, L.L., et al., 2014. Compression of pancreatic tumor blood vessels by hyaluronan is caused by solid stress and not interstitial fluid pressure. Cancer Cell 26 (1), 14–15.

Croft, C., 1969. Ultrastructural features of wound healing in mouse skin. J. Anat. 105, 189–190.

Desmouliere, A., Guyot, C., Gabbiani, G., 2004. The stroma reaction myofibroblast: a key player in the control of tumor cell behavior. Int. J. Dev. Biol. 48 (5–6), 509–517.

d'Esposito, A., Sweeney, P.W., Ali, M., Saleh, M., Ramasawmy, R., Roberts, T.A., Agliardi, G., Desjardins, A., Lythgoe, M.F., Pedley, R.B., et al., 2018. Computational fluid dynamics with imaging of cleared tissue and of in vivo perfusion predicts drug uptake and treatment responses in tumours. Nat. Biomed. Eng. 2 (10), 773–787.

Dhani, N., Serra, S., Pintilie, M., Schwock, J., Xu, J., Gallinger, S., Hill, R., Hedley, D., 2015. Analysis of the intra-and intertumoral heterogeneity of hypoxia in pancreatic cancer patients receiving the nitroimidazole tracer pimonidazole. Br. J. Cancer 113 (6), 864–871.

Dhani, N., Fyles, A., Hedley, D., Milosevic, M., 2015. The Clinical Significance of Hypoxia in Human Cancers in Seminars in Nuclear Medicine, vol. 45. Elsevier, pp. 110–121.

DuFort, C.C., DelGiorno, K.E., Carlson, M.A., Osgood, R.J., Zhao, C., Huang, Z., Thompson, C.B., Connor, R.J., Thanos, C.D., Brockenbrough, J.S., et al., 2016. Interstitial pressure in pancreatic ductal adenocarcinoma is dominated by a gel-fluid phase. Biophys. J . 110 (9), 2106–2119.

Evje, S., 2017. An integrative multiphase model for cancer cell migration under influence of physical cues from the microenvironment. Chem. Eng. Sci. 165, 240–259.

Evje, S., Waldeland, J.O., 2019. How tumor cells can make use of interstitial fluid flow in a strategy for metastasis. Cell. Mol. Bioeng. 12 (3), 227–254.

Feig, C., Gopinathan, A., Neesse, A., Chan, D.S., Cook, N., Tuveson, D.A., 2012. The pancreas cancer microenvironment. Clin. Cancer Res. 18 (16).

Fink, D.M., Steele, M.M., Hollingsworth, M.A., 2016. The lymphatic system and pancreatic cancer. Cancer Lett. 381 (1), 217–236.

Fischer, K.R., Durrans, A., Lee, S., Sheng, J., Li, F., Wong, S.T., Choi, H., El Rayes, T., Ryu, S., Troeger, J., et al., 2015. Epithelial-to-mesenchymal transition is not required for lung metastasis but contributes to chemoresistance. Nature 527 (7579), 472–476.

Fokas, E., O'Neill, E., Gordon-Weeks, A., Mukherjee, S., McKenna, W.G., Muschel, R.J., 2015. "Pancreatic ductal adenocarcinoma: from genetics to biology to radiobiology to oncoimmunology and all the way back to the clinic. Biochim. Biophys. Acta 1855 (1), 61–82.

Follain, G., Herrmann, D., Harlepp, S., Hyenne, V., Osmani, N., Warren, S.C., Timpson, P., Goetz, J.G., 2020. Fluids and their mechanics in tumour transit: shaping metastasis. Nat. Rev. Cancer 20, 107–124.

Frieboes, H., Jina, F., Chuang, Y.-L., Wise, S., Lowengrub, J., Cristini, V., 2010. Three-dimensional multispecies nonlinear tumor growth–ii: tumor invasion and angiogenesis. J. Theor. Biol. 264 (4), 1254–1278.

Fyles, A.W., Milosevic, M., Wong, R., Kavanagh, M.-C., Pintilie, M., Sun, A., Chapman, W., Levin, W., Manchul, L., Keane, T.J., et al., 1998. Oxygenation predicts radiation response and survival in patients with cervix cancer. Radiother. Oncol. 48 (2), 149–156.

Fyles, A., Milosevic, M., Pintilie, M., Syed, A., Levin, W., Manchul, L., Hill, R.P., 2006. Long-term performance of interstial fluid pressure and hypoxia as prognostic factors in cervix cancer. Radiother. Oncol. 80 (2), 132–137.

Gaggioli, C., Hooper, S., Hidalgo-Carcedo, C., Grosse, R., Marshall, J.F., Harrington, K., Sahai, E., 2007. Fibroblast-led collective invasion of carcinoma cells with

differing roles for rhogtpases in leading and following cells. Nat. Cell Biol. 9 (12), 1392–1400.

Giverso, C., Scianna, M., Grillo, A., 2015. Growing avascular tumours as elasto-plastic bodies by the theory of evolving natural configurations. Mech. Res. Commun. 68, 31–39.

Guo, J., Lou, W., Ji, Y., Zhang, S., 2013. Effect of ccr7, cxcr4 and vegf-c on the lymph node metastasis of human pancreatic ductal adenocarcinoma. Oncol. Lett. 5 (5), 1572–1578.

Hansem, L.M.K., Huang, R., Wegner, C.S., Simonsen, T.G., Gaustad, J.-V., Hauge, A., Rofstad, E.K., 2019. Intratumor heterogeneity in interstitial fluid pressure in cervical and pancreatic carcinoma xenografts. Transl. Oncol. 12 (8), 1079–1085.

Höckel, M., Vaupel, P., 2001. Biological consequences of tumor hypoxia. Semin. Oncol., vol. 28. Elsevier, pp. 36–41.

Höckel, M., Knoop, C., Schlenger, K., Vorndran, B., Baußnann, E., Mitze, M., Knapstein, P.G., Vaupel, P., 1993. Intratumoral po2 predicts survival in advanced cancer of the uterine cervix. Radiother. Oncol. 26 (1), 45–50.

Höckel, M., Schlenger, K., Aral, B., Mitze, M., Schäffer, U., Vaupel, P., 1996. Association between tumor hypoxia and malignant progression in advanced cancer of the uterine cervix. Cancer Res. 56 (19), 4509–4515.

Hompland, T., Ellingsen, C., Øvrebø, K.M., Rofstad, E.K., 2012. Interstitial fluid pressure and associated lymph node metastasis revealed in tumors by dynamic contrast-enhanced mri. Cancer Res. 72 (19), 4899–4908.

Hormuth, D.A., Jarrett, A.M., Feng, X., Yankeelov, T.E., 2019. Calibrating a predictive model of tumor growth and angiogenesis with quantitative mri. Ann. Biomed. Eng. 47 (7), 1539–1551.

Hubbard, M., Byrne, H.M., 2013. Multiphase modelling of vascular tumour growth in two spatial dimensions. J. Theor. Biol. 316, 70–89.

Jain, R.K., Martin, J.D., Stylianopoulos, T., 2014. The role of mechanical forces in tumor growth and therapy. Annu. Rev. Biomed. Eng. 16, 321–346.

Jarrett, A.M., Hormuth, D.A., Barnes, S.L., Feng, X., Huang, W., Yankeelov, T.E., 2018. Incorporating drug delivery into an imaging-driven, mechanicscoupled reaction diffusion model for predicting the response of breast cancer to neoadjuvant chemotherapy: theory and preliminary clinical results. Phys. Med. Biol. 63, 820–830.

Jarrett, A.M., II, D.A.H., Wu, C., Kazerouni, A.S., Ekrut, D.A., Virostko, J., Sorace, A.G., DiCarlo, J.C., Kowalski, J., Patt, D., Goodgame, B., Avery, S., Yankeelov, T.E., 2020. Evaluating patient-specific neoadjuvant regimens for breast cancer via a mathematical model constrained by quantitative magnetic resonance imaging data. Neoplasia 22, 820–830..

Kalli, M., Papageorgisa, P., Gkretsi, V., Stylianopoulos, T., 2018. Solid stress facilitates fibroblasts activation to promote pancreatic cancer cell migration. Ann. Biomed. Eng. 46 (5), 657–669.

Kalluri, R., Zeisberg, M., 2006. Fibroblasts in cancer. Nat. Rev. Cancer 6 (5), 392–401.

Klopp, A.H., Eifel, P.J., 2012. Biological predictors of cervical cancer response to radiation therapy. Seminars in Radiation Oncology, vol. 22. Elsevier, pp. 143–150.

Kramer, B., de Haan, L., Vermeer, M., Olivier, T., Hankemeier, T., Vulto, P., Joore, J., Lanz, H.L., 2019. Interstitial flow recapitulates gemcitabine chemoresistance in a 3d microfluidic pancreatic ductal adenocarcinoma model by induction of multidrug resistance proteins. Int. J. Mol. Sci. 20, 1–18.

Labernadie, A., Kato, T., Brugués, A., Serra-Picamal, X., Derzsi, S., Arwert, E., Weston, A., González-Tarragó, V., Elosegui-Artola, A., Albertazzi, L., et al., 2017. A mechanically active heterotypic e-cadherin/n-cadherin adhesion enables fibroblasts to drive cancer cell invasion. Nat. Cell Biol. 19 (3), 224–237.

Lakiotaki, E., Sakellariou, S., Evangelou, K., Liapis, G., Patsouris, E., Delladetsima, I., 2016. Vascular and ductal elastotic changes in pancreatic cancer. APMIS 124 (3), 181–187.

Lewin, T.D., Maini, P.K., Moros, E.G., Enderling, H., Byrne, H.M., 2020. A three phase model to investigate the effects of dead material on the growth of avascular tumours. Math. Model. Nat. Phenomena 15 (22).

Lunt, S.J., Fyles, A., Hill, R.P., Milosevic, M., 2008. Interstitial fluid pressure in tumors: therapeutic barrier and biomarker of angiogenesis. Future Oncol. 4 (6).

Mahadevan, D., Von Hoff, D.D., 2007. Tumor-stroma interactions in pancreatic ductal adenocarcinoma. Mol. Cancer Ther. 6 (4), 1186–1197.

Mascheroni, P., Stigliano, C., Carfagna, M., Boso, D.P., Preziosi, L., Decuzzi, P., Schrefler, B.A., 2016. Predicting the growth of glioblastoma multiforme spheroids using a multiphase porous media model. Biomech. Model Mechanobiol. 15, 1215–1228.

Mascheroni, P., Boso, D., Preziosi, L., Schrefler, B.A., 2017. Evaluating the influence of mechanical stress on anticancer treatments through a multiphase porous media model. J. Theor. Biol. 421, 179–188.

Mascheroni, P., Alfonso, J.C.L., Kalli, M., Stylianopoulos, T., Meyer-Hermann, M., Hatzikirou, H., 2019. On the impact of chemo-mechanically induced phenotypic transitions in gliomas. Cancers 11, 716.

Milosevic, M., Fyles, A., Hedley, D., Pintilie, M., Levin, W., Manchul, L., Hill, R., 2001. Interstitial fluid pressure predicts survival in patients with cervix cancer independent of clinical prognostic factors and tumor oxygen measurements. Cancer Res. 61 (17), 6400–6405.

Mpekris, F., Angeli, S., Pirentis, A.P., Stylianopoulos, T., 2015. Stress-mediated progression of solid tumors: effect of mechanical stress on tissue oxygenation, cancer cell proliferation and drug delivery. Biomech. Model Mechanobiol. 14 (6), 1391–1402.

Onozato, M.L., Kovach, A.E., Yeap, B.Y., Morales-Oyarvide, V., Klepeis, V.E., Tammireddy, S., Heist, R.S., Mark, E.J., Dias-Santagata, D., Iafrate, A.J., et al., 2013. Tumor islands in resected early stage lung adenocarcinomas are associated with unique clinicopathological and molecular characteristics and worse prognosis. Am. J. Surg. Pathol. 37 (2), 287.

Polacheck, W.J., Charest, J.L., Kamm, R.D., 2011. Interstitial flow influences direction of tumor cell migration through competing mechanisms. In: Proc. Natl. Acad. Sci., pp. 11115–11120.

Polacheck, W.J., German, A.E., Mammoto, A., Ingber, D.E., Kamm, R.D., 2014. Mechanotransduction of fluid stresses governs 3d cell migration. In: Proc. Natl. Acad. Sci., pp. 2447–2452.

Provenzano, P.P., Cuevas, C., Chang, A.E., Goel, V.K., Von Hoff, D.D., Hingorani, S.R., 2012. Enzymatic targeting of the stroma ablates physical barriers to treatment of pancreatic ductal adenocarcinoma. Cancer Cell 21 (3), 418–429.

Qiao, Y., Evje, S., 2020. A compressible viscous three-phase model for porous media flow based on the theory of mixtures. Adv. Water Resour. 141.

Qiao, Y., Andersen, P.O., Evje, S., Standnes, D., 2018. A mixture theory approach to model co-and counter-current two-phase flow in porous media accounting for viscous coupling. Adv. Water Resour. 112, 170–188.

Rahman, M.M., Feng, Y., Yankeelov, T.E., Oden, J.T., 2017. A fully coupled space–time multiscale modeling framework for predicting tumor growth. Comput. Methods Appl. Mech. Eng. 320, 261–286.

Schwager, S.C., Taufalele, P.V., Reinhart-King, C.A., 2019. Cell–cell mechanical communication in cancer. Cell. Mol. Bioeng. 12 (1), 1–14.

Schwickert, G., Walenta, S., Sundfør, K., Rofstad, E.K., Mueller-Klieser, W., 1995. Correlation of high lactate levels in human cervical cancer with incidence of metastasis. Cancer Res. 55 (21), 4757–4759.

Shieh, A.C., Rozansky, H.A., Hinz, B., Swartz, M.A., 2011. Tumor cell invasion is promoted by interstitial flow-induced matrix priming by stromal fibroblasts. Cancer Res. 71 (3), 790–800.

Singh, D., Upadhyay, G., Srivastava, R.K., Shankar, S., 2015. "Recent advances in pancreatic cancer: biology, treatment, and prevention. Biochim. Biophys. Acta 1856 (1), 13–27.

Sperveslage, J., Frank, S., Heneweer, C., Egberts, J., Schniewind, B., Buchholz, M., Bergmann, F., Giese, N., Munding, J., Hahn, S.A., et al., 2012. Lack of ccr7 expression is rate limiting for lymphatic spread of pancreatic ductal adenocarcinoma. Int. J. Cancer 131 (4), E371–E381.

Sundfør, K., Lyng, H., Tropé, C.G., Rofstad, E.K., 2000. Treatment outcome in advanced squamous cell carcinoma of the uterine cervix: relationships to pretreatment tumor oxygenation and vascularization. Radiother. Oncol. 54 (2), 101–107.

Urdal, J., Waldeland, J.O., Evje, S., 2019. Enhanced cancer cell invasion caused by fibroblasts when fluid flow is present. Biomech. Model. Mechanobiol. 18 (4), 1047–1078.

Vaupel, P.W., Kelleher, D.K., 2012. Blood flow and associated pathophysiology of uterine cervix cancers: characterisation and relevance for localised hyperthermia. Int. J. Hyperth. 28 (6), 518–527.

Von Ahrens, D., Bhagat, T.D., Nagrath, D., Maitra, A., Verma, A., 2017. The role of stromal cancer-associated fibroblasts in pancreatic cancer. J. Hematol. Oncol. 10 (1), 76.

Waldeland, J.O., Evje, S., 2018. Competing tumor cell migration mechanisms caused by interstitial fluid flow. J. Biomech. 81, 22–35.

Waldeland, J.O., Polacheck, W.J., Evje, S., 2020. Collective tumor cell migration in the presence of fibroblasts. J. Biomech. 100.

Walenta, S., Wetterling, M., Lehrke, M., Schwickert, G., Sundfør, K., Rofstad, E.K., Mueller-Klieser, W., 2000. High lactate levels predict likelihood of metastases, tumor recurrence, and restricted patient survival in human cervical cancers. Cancer Res. 60 (4), 916–921.

Weis, J.A., Miga, M.I., Arlinghaus, L.R., Li, X., Abramson, V., Chakravarthy, A.B., Pendyala, P., Yankeelov, T.E., 2015. Predicting the response of breast cancer to neoadjuvant therapy using a mechanically coupled reaction-diffusion model. Cancer Res. 75 (22), 4697–4707.

Weis, J.A., Miga, M.I., Arlinghaus, L.R., Li, X., Abramson, V., Chakravarthy, A.B., Pendyala, P., Yankeelov, T.E., 2015. Predicting the response of breast cancer to neoadjuvant therapy using a mechanically coupled reaction–diffusion model. Cancer Res. 75 (22), 4697–4707.

Weis, J.A., Miga, M.I., Yankeelov, T.E., 2017. Three-dimensional image-based mechanical modeling for predicting the response of breast cancer to neoadjuvant therapy. Comput. Methods Appl. Mech. Eng. 314, 494–512.

Whatcott, C.J., Diep, C.H., Jiang, P., Watanabe, A., LoBello, J., Sima, C., Hostetter, G., Shepard, H.M., Von Hoff, D.D., Han, H., 2015. Desmoplasia in primary tumors and metastatic lesions of pancreatic cancer. Clin. Cancer Res. 21 (15), 3561–3568.

Wiig, H., Swartz, M.A., 2012. Interstitial fluid and lymph formation and transport: physiological regulation and roles in inflammation and cancer. Physiol. Rev. 92 (3), 1005–1060.

Winter, J.M., Brennan, M.F., Tang, L.H., D'Angelica, M.I., DeMatteo, R.P., Fong, Y., Klimstra, D.S., Jarnagin, W.R., Allen, P.J., 2012. Survival after resection of pancreatic adenocarcinoma: results from a single institution over three decades. Ann. Surg. Oncol. 19 (1), 169–175.

Wu, M., Frieboes, H.B., McDougall, S.R., Chaplain, M.A.J., Cristini, V., Lowengrub, J., 2013. The effect of interstitial pressure on tumor growth: coupling with the blood and lymphatic vascular systems. J. Theor. Biol. 320, 131–151.

Wu, M., Frieboes, H.B., McDougall, S.R., Chaplain, M.A.J., Cristini, V., Lowengrub, J., 2014. The effect of interstitial pressure on therapeutic agent transport: coupling with the tumor blood and lymphatic vascular systems. J. Theor. Biol. 355, 194–207.

Yan, H., Romero-Lopez, M., Benitez, L.I., Di, K., Frieboes, H.B., Hughes, C.C., Bota, D.A., Lowengrub, J.S., 2017. 3d mathematical modeling of glioblastoma suggests that transdifferentiated vascular endothelial cells mediate resistance to current standard-of-care therapy. Cancer Res. 77 (15), 4171–4184.

Yeo, S.-G., Kim, J.-S., Cho, M.-J., Kim, K.-H., Kim, J.-S., 2009. Interstitial fluid pressure as a prognostic factor in cervical cancer following radiation therapy. Clin. Cancer Res. 15 (19), 6201–6207.

Zheng, X., Carstens, J.L., Kim, J., Scheible, M., Kaye, J., Sugimoto, H., Wu, C.-C., LeBleu, V.S., Kalluri, R., 2015. Epithelial-to-mesenchymal transition is dispensable for metastasis but induces chemoresistance in pancreatic cancer. Nature 527 (7579), 525–530.